DOCTORAL THESIS

Tumour vasculature, oxygenation and radiosensitivity

A numerical modelling study

Jakob H. Lagerlöf

A thesis submitted in fulfilment of the requirements
for the degree of Doctor of Philosophy

in the

Department of Radiation Physics
The Sahlgrenska Academy

2014

UNIVERSITY OF GOTHENBURG

Cover illustration:
Sum image of three-dimensional segmented vascular structure from a 168 μm thick sample of tumour tissue (insulinoma), reconstructed from 12 μm slices.

Tumour vasculature, oxygenation and radiosensitivity

A numerical modelling study

jakob@radfys.gu.se

ISBN 978-91-637-5257-5

URL http://hdl.handle.net/2077/34840

"En del människor verkar ägna sin tid åt att vara trevliga istället för att försöka förstå."
Naima Lagerlöf, 10 år

"Good judgement comes from experience, experience comes from bad judgement."
Mark Twain

Abstract

This thesis aims to investigate theoretically how parameters such as vessel density, blood oxygenation, blood velocity, spatial oxygen variation along vessels, tissue oxygen consumption and their distributions influence the radiosensitivity of tumours.

Numerical calculations are made in MATLAB using voxel-based models. Direct and indirect Monte Carlo based methods are used, e.g. kernels for dose calculations and random-based models for simulation of in oxygen and activity distributions in tumours. Oxygen diffusion is calculated using a Green's function based method and oxygen consumption follows the Michaelis-Menten kinetic model. Cryosectioning and immunostaining of insulinoma from mouse is done for model development. The linear quadratic cell survival model , including the oxygen effect, is used to calculate tumour control probability (TCP) and absorbed doses. Convolutions, with diffusion and dose kernels, are preferably made in frequency space for computational reasons.

By raising the oxygen pressure (pO_2), through antiangiogenic treatment, in tumours and retaining TCP, radiation damage to normal tissues can be strongly reduced. Variation of blood pO_2 affects the position of the pO_2 distribution while altered vessel density affects the distribution shape. The greatest increase in radiosensitivity by increased pO_2 is achieved for 50% relative vessel density. In tumour oxygenation modelling, pO_2 of the blood must vary along the vessel and a random distribution of pO_2 in incoming blood is used to get realistic results.

Combining improved oxygenation and radionuclide uptake shows great potential of improving radionuclide treatment. There is an optimum region of vessel density where the highest increase in radiosensitivity is achieved by increasing blood pO_2. It appears to be possible to determine the cause of hypoxia from the shape of the pO_2 distribution. To make a good estimate of treatment result, it is crucial to know the full pO_2 distribution and not only the mean or the hypoxic fraction. Improving oxygenation of partly necrotic tumours is not always beneficial for radiation treatment.

Small spherical tumours are more sensitive than larger ones to the shape of the pO_2 distribution. This is likely because a hypoxic region of a small tumour is more affected by its location relative to the tumour centre, given constant thickness, due to the relatively greater difference in radius and therefore volume.

Sammanfattning

Denna avhandling syftar till att kartlägga hur olika parametrar såsom kärltäthet, syrenivå i blodet, blodets hastighet i kärlen, syrevariation längs med kärlen, syrekonsumtion i vävnaden och hur fördelningen av dessa parametrar och korrelation mellan dem påverkar strålningskänsligheten hos tumörer. Beräkningarna utförs med numeriska, voxelbaserade, modeller i MATLAB. Direkta och indirekta Monte Carlo-baserade metoder används, såsom kernlar för dosberäkningar och slumpbaserade modeller för simulering av variation av syrenivåer och aktivitetsfördelning i tumörer. För beräkning av syrediffusion används Greens function-metoder och för syrekonsumtionen används Michaelis-Mentens kinetikmodell. Fryssnitt och infärgning görs av insulinom från mus, som underlag för modellutveckling. Den linjärkvadratiska modellen för cellöverlevnad, inklusive syreeffekten, används för beräkning av tumour control probability (TCP) och növändiga stråldoser. Faltning, med diffusions- och doskernlar, sker mestadels i frekvensrummet av beräkningstekniska skäl.

Genom en höjning av syretrycket (pO_2), genom behandling med antiangiogenetika, i tumörer och bibehållen TCP kan man kraftigt minska skadeeffekter på normalvävnad vid bestrålning. Variation av pO_2 i blodet påverkar syrefördelningens läge medan ändring av kärltäthet påverkar formen. Den största strålningskänslighetshöjande effekten av höjt pO_2 åtstadkoms vid halverad kärltäthet. Vid modellering av syrefördelning i tumörer måste pO_2 i blodkärlen varieras logitudinellt och en slumpmässig fördelning av pO_2 i inkommande blod tillämpas för att få verklighetstrogna syrefördelningar.

En kombinerad höjning av syreupptag och radionuklider ger stor förbättringspotential vid radionuklidbehandling. Det finns ett optimalt spann av kärltäthet för att nå maximal strålkänslighetshöjande effekt av ökad syrenivå i blodet. Det förefaller också vara möjligt att skilja mellan olika typer av hypoxi utifrån syrefördelningens form. För att prognostisera resultat av bestrålning är det nödvändigt att känna till hela syrefördelningen och inte bara medelnivån eller den hypoxiska fraktionen. Förbättrad syresättning av tumörer med nekrotiska fraktioner ger inte alltid bättre förutsättningar för bestrålning, såsom i fallet för icke nekrotiska tumörer. Små sfäriska tumörer tenderar att vara känsligare än stora för syrefördelningens form. Detta bör bland annat bero på att en hypoxisk region i en mindre tumör påverkas mer av sitt läge relativt tumörens centrum än vad som är fallet i en större tumör givet konstant tjocklek, på grund av den relativt större skillnaden i radie och därmed volym.

List of papers

This thesis is based on the following studies, referred to in the text by their Roman numerals.

I J.H. Lagerlöf, J. Kindblom and P. Bernhardt, "3D modeling of effects of increased oxygenation and activity concentration in tumors treated with radionuclides and antiangiogenic drugs", Medical Physics, Volume 38, Issue 8, Pages 4888-93, 2011

II J.H. Lagerlöf, J. Kindblom, E. Cortez, K. Pietras and P. Bernhardt, "Image-based 3D modeling study of the influence of vessel density and blood hemoglobin concentration on tumor oxygenation and response to irradiation", Medical Physics, Volume 40, Issue 2, Pages 024101:1-7
Featured by Global Medical Discovery [ISSN 1929-8536]
Featured by World Biomedical Frontiers [ISSN 2328-0166]

III J.H. Lagerlöf, J. Kindblom and P. Bernhardt, "The impact of including spatially longitudinal heterogeneities of vessel oxygen content and vascular fraction in 3D tumour oxygenation models on predicted radiation sensitivity", Accepted for publication in Medical Physics, February 2014

IV J.H. Lagerlöf, J. Kindblom and P. Bernhardt, "Oxygen distribution in tumours - a qualitative analysis and modelling study providing a novel Monte Carlo approach", Submitted for publication in Medical Physics, 2014

The following papers have been published, but are not included in the thesis

- E. Wikberg, P. Bernhardt, G. Maltese, P. Tarnow, J.H. Lagerlöf and L. Kölby. "A new computer tool for systematic evaluation of intracranial volume and its capacity to evaluate the result of the operation for metopic synostosis", J Plast Surg Hand Surg. 2012 Dec; 46(6):393-8.

- P. Bernhardt, A. Lindström, G. Maltese, P. Tarnow, J.H. Lagerlöf and L. Kölby. "A novel quantitative image-based method for evaluating cranial symmetry and its usefulness in patients undergoing surgery for unicoronal synostosis", J Craniofac Surg. 2013 Jan; 24(1):166-9.

- G. Maltese, P. Tarnow, E. Wikberg, P. Bernhardt, J.H Lagerlöf, R. Tovetjärn and L. Kölby. "Intracranial volume before and after surgical treatment for isolated metopic synostosis", J Craniofac Surg. 2014 Jan;25(1):262-6.

- G. Maltese, P. Tarnow, A. Lindström, J.H Lagerlöf, P. Bernhardt, R. Tovetjärn and L. Kölby. "New objective measurement of forehead symmetry in unicoronal craniosynostosis - comparison between fronto-orbital advancement and forehead remodelling with a bone graft", J Plast Surg Hand Surg. 2014 Feb; 48(1):59-62.

The following presentations, of preliminary results, have been given

- "Simulation of combinatorial effects after chemotherapy and radiotherapy of glioblastoma multiforme", Society of Nuclear Medicine annual meeting, Toronto 2009, Poster presentation.

- "Simulation of tumour response to combinatorial treatment of radiopharmaceuticals and angiogenesis inhibitors", Swedish Cancer Society Planning Group for Radionuclide Therapy annual meeting, Gothenburg 2009, Oral presentation (swedish).

Contents

List of Figures

List of Tables

Abbreviations

BSA	**B**ovine **S**erum **A**lbumin
CSDA	**C**ontinous **S**lowing **D**own **A**proximation
DOC	**D**epth **O**xygenation **C**urve
$\mathbf{D_{99}}$	Absorbed **D**ose at TCP=0.**99**
FFT	**F**ast **F**ourier **T**ransform
GBM	**G**lio**B**lastoma **M**ultiforme
Hb	**H**aemoglo**b**in
HF	**H**ypoxoc **F**raction
IP	**I**nterstitial **P**ressure
LQ	**L**inear **Q**uadratic
mAb	**m**onoclonal **A**nti**b**ody
MC	**M**onte **C**arlo
MRI	**M**agnetic **R**esonance **I**maging
ODA	**O**xygenation-induced **D**ose **A**mplification
OED	**O**xygen **E**ffective **D**ose
OER	**O**xygen **E**nhancement **R**atio
PBS	**P**hosphate-**B**uffred **S**aline
pdf	**p**robability **d**ensity **f**unction
PET	**P**ositron **E**mission **T**omography
$\mathbf{pO_2}$	partial **O**xygen **p**ressure
RCC	**R**enal **C**ell **C**arcinoma
RMSD	**R**oot **M**ean **S**quare **D**eviation
SD	**S**tandard **D**eviation
TCP	**T**umour **C**ontrol **P**robability

TNC	**T**umour-to-**N**ormal tissue activity **C**oncentration ratio
UP	**U**ncorrelated **P**arameters
VF	**V**ascular **F**raction
VEGF	**V**ascular **E**ndothelial **G**rowth **F**actor
VPO-C	**V**essel **P**roximity **O**xygen negative **C**ovariance
VPO+C	**V**essel **P**roximity **O**xygen positive **C**ovariance
3D	**3**-**D**imensional

Symbols

c	Concentration/probability	
C	Oxygen consumption	mm Hg s^{-1}
D	Absorbed dose	Gy
D_O	Diffusion coefficient of oxygen in tissue	μm^2 s^{-1}
j	Volumetric blood flux	μms^{-1}
k	Normalisation constant	
K_M	Michealis constant	mm Hg
N	Number of tumour cells	
O	Partial oxygen pressure	mm Hg
r^2	Coefficient of determination	
R^2	Coefficient of determination	
v_{blood}	Blood velocity	μms^{-1}
vd	Intercapillary spacing/vessel proximity	μm
vf	Vascular fraction	

α	Linear radiation sensitivity parameter	Gy^{-1}
β	Quadratic radiation sensitivity parameter	Gy^{-2}
δ	Kronecker delta	
μ	Mean value	
σ	Standard deviation	

To
my wife Elin and my children: David, Naima, Tore and Karin

Chapter 1

Introduction

There is nothing difficult about killing a tumour with radiation. The challenge is doing it without killing the entire patient or causing the patient avoidable damage. This is what motivates research on radiation treatment against cancer. Mathematical modelling may provide an efficient way of estimating the influence of different properties. Like English statistician George Box said: *"Remember that all models are wrong; the practical question is how wrong do they have to be to not be useful"*.[1] Our intention is to make them sufficiently accurate for some conclusions about reality to be drawn. In this section I will explain some of the principles, theories and assumptions that provide the basis of the models described in this thesis.

1.1 Tumour control and the oxygen effect

If we had only the tumour to worry about, the entire process would be a simple matter of delivering an absorbed dose high enough to kill it, but since the tumour is inside the patient, radiation will have to pass through healthy tissue on its way to its target. Unfortunately, healthy tissue is generally just as sensitive to radiation as tumour tissue. In this context, the concept of tumour control becomes interesting. Tumour control means killing every cell of the tumour and tumour control probability (TCP) is the probability of killing every cell of the tumour, obviously.

There are ways to estimate TCP and the most widely used is the Linear-Quadratic cell survival model (LQ-model). The expression reads thusly:

$$SF = e^{-(\alpha D+\beta D^2)}. \tag{1.1}$$

SF is the surviving fraction of a population of cells exposed do the absorbed dose D (Gy). For a single cell SF may be interpreted as the probability of survival. α and β are radiation sensitivity parameters that are specific to each tumour type and possibly even to each individual tumour. What makes radiation toxic to cells is its ability to irreparably destroy their DNA, stopping them from proliferating and causing them to self-terminate. The probability of radiation to cause damage to (hit) DNA is considered proportional to absorbed dose. The fundamental assumption of the LQ-model is that irreparable damage to DNA may require one or two hits. α and $\sqrt{\beta}$ may then be thought of as probabilities in some sense per unit of absorbed dose for a lethal damage to be caused by one or two hits. The values of α and β and the relationship between them is an interesting matter when it comes to strategies for dose delivery. In essence, when radiation is delivered slowly, single hit processes dominate cell killing and vice versa, since there are continuous damage repair processes taking place in the cells.[2]

If SF is the surviving fraction of a population of cells, then $1-SF$ is the non-surviving fraction. Consequently on a cellular level, if SF may be interpreted as the probability of survival, then $1-SF = 1-e^{-(\alpha D+\beta D^2)}$ may be interpreted as the probability of non-survival. Assuming that we have a population of N tumour cells, then the probability of none of them surviving the dose D is $(1-SF_1)(1-SF_2)\cdots(1-SF_N)$ which, if the cells are identical, equals

$$(1-SF)^N = \left(1-e^{-(\alpha D+\beta D^2)}\right)^N. \tag{1.2}$$

This is the TCP. The absorbed dose for which TCP is 0.99 is called D_{99}.

Oxygen plays an important role in the process of destroying DNA.[3] If irradiation occurs in the presence of oxygen, oxygen molecules are dissociated, forming highly reactive radicals.[4] When DNA is hit, before repair processes have initiated, oxygen radicals bind to the damaged molecule, fixate the damage and prevent reparation from taking place. Under these circumstances, the same level of cell kill can be accomplished at a lower absorbed dose. This oxygen enhancement increases the effect of the radiation up to three-fold for well oxygenated compared to anoxic cells.[3] This has been experimentally confirmed by Carlson et al.[5] This effect is important only

with sparsely ionising radiation, since the damage caused by densely ionising radiation is too extensive for reparation. When the oxygen enhancement ratio (OER) is included in the TCP-formulation, the expression becomes

$$(1-SF)^N = \left(1-e^{-(\alpha OER\cdot D+\beta(OER\cdot D)^2)}\right)^N. \tag{1.3}$$

1.2 Brownian motion and diffusion

In 1827, Scottish botanist Robert Brown was looking at pollen grains in his microscope and noticed that they were moving back and forth in the water surrounding them. This phenomenon, which at the time nobody was able to explain, was named Brownian motion.[6] It remained a mystery until Albert Einstein in 1905 concluded that the particle movements were caused by constant collisions with molecules in the liquid, due to their thermal vibration. Because these collisions occur very often, the result of individual collisions is not observable, but the particle trajectory will be the sum of many consecutive collisions that may be regarded as independent of each other (random). According to the central limit theorem, the sum of many random events, of the same distribution, will follow a normal (Gaußian) distribution.[7] This means that a particle in a gas or fluid will, during each macroscopic time step move some distance. The probability of the distance travelled is distributed according to the Gaußian function. If there are many particles, the particle concentration, in the volume surrounding each source of particles, will follow the same distribution. Although there are exotic circumstances under which these assumptions are not valid,[8] this line of reasoning holds for a majority of applications, of which oxygen transport in tissue is one. This transport phenomenon is known as diffusion. If the transport conditions in a medium are homogeneous, the distribution will be constant in space (different of course for each particle type due to size, weight etc.). Diffusion always causes a net transportation from higher to lower concentrations. This was described by Adolf Fick already in 1855, and is known as Fick's first law of diffusion.[9]

Diffusion is governed by the diffusion equation, a partial differential equation, which in an environment that is homogeneous with respect to diffusion is written

$$\frac{\partial}{\partial t}c(\mathbf{r},t) = D\nabla^2 c(\mathbf{r},t), \tag{1.4}$$

(also known as the heat equation), where D is the diffusion coefficient (or thermal conductivity), a material specific parameter, essentially the velocity of the diffusing substance and c is the concentration (or temperature) and ∇^2 is the laplace operator, which is the same as the sum of all second order partial derivatives (in this case $\mathbf{r} = (x, y, z)$ so $\nabla^2 = \left(\frac{\partial^2}{\partial x^2} + \frac{\partial^2}{\partial y^2} + \frac{\partial^2}{\partial z^2}\right)$). In many situations, the diffusion equation may be solved analytically if the circumstances are right. In many situations, however, this is tedious or even impossible and in those situation one can make use of the Gaußian function, which is a solution to the diffusion equation, to come up with a numerical solution. The Gaußian is

$$c(r, t) = k \cdot t^{-\frac{3}{2}} \cdot e^{-\frac{1}{4Dt} r^2}. \tag{1.5}$$

k is a normalisation constant, t is time and in three dimensions, $r = \left(x^2 + y^2 + z^2\right)^{\frac{1}{2}}$.[10]

1.3 Oxygen transport

In the blood, haemoglobin (Hb) acts as a buffer of oxygen. Haemoglobin binds an amount of oxygen (forming oxyhaemoglobin, $Hb(O_2)_4$) that depends on the oxygen partial pressure of the blood, so that, in well oxygenated blood, all but a few per cent of the oxygen in the blood is bound. As free oxygen diffuses from the blood, the equilibrium changes and oxyhaemoglobin dissociates, releasing more oxygen into the plasma. This feature drastically increases the oxygen transportation capacity of the blood, evens the oxygen levels of tissue and reduces sensitivity to variations in the inspired oxygen concentration. Since nearly all oxygen in the blood is bound to haemoglobin, the concentration of haemoglobin (Hb value) is essentially proportional to the oxygen transportation capacity of the blood. Normal Hb value is around 14 g per 100 ml of blood and every gram of Hb carries a maximum of 1.34 ml of oxygen.[11]

The volumetric oxygen concentration in dry air is 20.93%. At an air pressure of 760 mmHg, this corresponds to a pO_2 of 159 mmHg. When air is inhaled it becomes warmer and saturates with water vapor (pH_2O=47 mmHg), leading to a relative decrease in oxygen content and a pO_2 of 149 mmHg.[12,13] This is what applies to the air that enters the lungs with every breath. Since the ventilation of the lungs is not complete and due to the dead space, there is always residual air, further lowering the pO_2 in the lungs. Inside the alveoli, where gas exchange between air and blood

takes place, the oxygen pressure is fairly constant at an average of 104 mmHg due to simultaneous supply of oxygen through limited alveolar ventilation and removal to the blood. While the partial pressure of a gas in gas simply is its contribution the total pressure, the partial pressure of a gas in liquid is determined by its solubility; the higher the solubility, the lower the partial pressure for equal concentrations.

The alveoli are very small, on the order of 200 μm, hence with a large surface area per volume. They are essentially covered in pulmonary capillaries, with poorly oxygenated (about 40 mmHg) blood slowly passing by. The initial pressure difference of around 64 mmHg will cause oxygen to rapidly diffuse from alveoli to capillaries. As the difference decreases, so will the diffusion rate. When the blood leaves the lungs, oxygen pressure will nearly have reached equilibrium and therefore be almost 104 mmHg. Hereafter, the blood leaves the lungs, moves towards the heart and combines with blood that has provided oxygen to lung tissue, not reached by inspired air, to an oxygen pressure of about 95 mmHg.[11]

After passing the heart, the blood enters the arterial system and is transported through a number of bifurcations to reach capillaries in the entire body. The capillaries are permeable, allowing for fluids to pass through the vessel walls to and from the extracellular space. Since the concentration of oxygen is higher inside the vessel than outside, diffusion will cause a net transport of oxygen into the tissue. On its way towards areas of lower concentration, oxygen will gradually be consumed by the cells, as they strive to perform whatever task they were assigned, since the oxygen is necessary for the cells to exercise their metabolism and thereby gain energy and dispose of garbage. Oxygen consumption varies between tissue types. This will affect the distance that oxygen can diffuse and in consequence, the capillaries will be spaced accordingly so that, in healthy tissues, the oxygen requirements of all cells are met.[14]

1.4 Tumour growth, vasculature and angiogenesis

Blood vessels have the purpose of delivering oxygen and nutrients to, and waste from, the entire body. The blood starts in the aorta, continues through the smaller arteries and via arterioles to the capillaries. On the venous side, the capillaries turn into venules, veins and finally the venae cavae. The exchange of nutrients and waste occurs in the capillary network. While the capillary wall is highly permeable to liquids and small molecules, larger molecules cannot pass. Through pressure differences, liquid is drawn out of the capillary and into the interstitium on the arterial end

until the pressure evens. Then, due to the excess of large molecules, plasma proteins, inside the capillary, an osmotic pressure is built up, forcing liquid to return to the capillaries and continue its journey back to the heart. Excessive fluid and escaped proteins are transported back to the heart by the lymphatic system. As previously mentioned, different types of tissue have different oxygen demands and the distance between capillaries is individually regulated for each type of tissue. There are several ways to quantify vascularisation. Vascular density may be expressed as vessels/mm^2, mean vessel distance or vessel proximity (μm) is sometimes used as well as vascular fraction, which is total vessel volume in relation to the tissue volume. These measures are not fully interchangeable since for example the oxygen distribution in tissue is highly dependent on the distance between vessels while flow resistance varies strongly with vessel diameter.[11]

The above description applies to tissues with a normal vascular system. In tumours, however, there is a different situation. Because tumours expand while their blood vessels essentially do not, they eventually outgrow their vascular supply; more tumour cells are added, contributing to a higher oxygen consumption, and the distance between microvessels changes as they are pushed apart by the tumour tissue. This causes insufficient oxygenation (hypoxia) among the tumour cells. Lack of nutrients due to poor blood supply (ischaemia) as well as long-lasting hypoxia may cause the cells irreparable damage and lead to uncontrolled cell death (necrosis). It is common for larger tumours to have one or several necrotic regions.[15,16]

Tumours grow through division of cells and with proper supply of nutrients and oxygen, the entire cell population is able to divide which makes the growth rate proportional to tumour volume,

$$\frac{\partial V}{\partial t} = SGR \cdot V \tag{1.6}$$

and thus the growth is exponential

$$V(t) = V_0 e^{SGR \cdot (t - t_0)}, \tag{1.7}$$

where $V(t)$ is the tumour volume at time t, V_0 is the volume at time t_0 and SGR is the specific growth rate (time^{-1}) of the tumour. Once the tumour becomes partly hypoxic, ischaemic or necrotic, not all of the cells contribute to the growth, which

becomes damped and no longer fits the purely exponential growth as in equation 1.7, but rather a size-limited model such as the Gomperzian which has a sigmoid growth curve; the shape is exponential at first, but then the tumour asymptotically approaches a maximum size.[17]

In order to continue to expand rapidly, the tumours need a way of overcoming ischaemia. When a tumour cell becomes hypoxic, this activates the secretion of angiogenic factors from the cell. These factors are a form of signal peptides, of which the vascular endothelial growth factor (VEGF) is an important example, that trigger angiogenesis. Angiogenesis is a process of vessel formation, first described by American pathologist Arthur Tremain Hertig already in 1935,[18] that has an important role for example in wound healing and in forming the placenta. What happens in the tumour when angiogenesis is stimulated is that existing vessels develop holes in the lumen and new vessels grow like sprouts from the existing vessels towards the hypoxic areas from where the signal substances originate. Because in larger tumours hypoxia is not generally concentrated only to a small volume, the angiogenic factors do not come from a point source, but from a larger region. This leads to a chaotic organisation of the new vascular structure with poorly functioning vessels. In addition, angiogenesis makes the existing vessels leaky and increasingly permeable to all sorts of molecules, which is bad since it destroys the vessels ability to reabsorb fluids through osmotic pressure difference.[11,14]

Due to the dysfunctional vessels of the tumour, the ingenious regulation system for fluid exchange between capillaries and the interstitium becomes ruined. This, in combination with inadequate venous and lymphatic drainage, results in elevated interstitial pressure, with impairment of perfusion as a consequence. It is possible to counteract angiogenesis by inhibition of receptors for angiogenic factors. This treatment can temporarily reduce the interstitial fluid pressure in the tumour and increase perfusion and thereby drug uptake and treatment effect.[16,19–22]

1.5 The Monte Carlo method

Stanislaw Ulam was a mathematician of Polish origin who, in 1946, started working in the Manhattan project for Los Alamos National Laboratory in the USA. Within this project, the first atomic bomb was developed. When Ulam was playing “Canfield solitaire” (a form of patience) the same year he started thinking about the probability of winning the game. He discovered the hard work of theoretically working

out all possible outcomes and figured there had to be a less time consuming way of estimation, for example by playing the game a hundred times. By this time, the computer evolution had set off and Ulam realised that computers could utilise the same method to make various sorts of calculations. He presented the idea to his colleague, John von Neumann, and together they started planning calculations on neutron diffusion. In order to keep the project a secret at first, they needed a code name and von Neumann suggested the name "Monte Carlo" after the casino where Ulams uncle gambled with borrowed money.[23]

The Monte Carlo method is still widely used today, within economics, physics and mathematics to solve problems that are impossible, excessively laborious or time consuming to master analytically. Within radiation physics we use the method mainly to predict how different types of particles interact with their surroundings. Instead of measuring, we can use probabilities and cross-sections to calculate how the particles will behave. About individual particles we can say nothing but about many we can say a lot. The more the particles, the more accurate the estimate, but accuracy has a price; simulation times increases with the number of particles.

When sampling from a distribution one may choose between two main methods: the rejection method and the inverse transform method. The two may also be combined into something called mixed methods, useful for sampling functions of several stochastic variables. The rejection method is very effective (all samples are approved) but requires that the probability density function (pdf), $f(x)$, can be integrated to form the distribution function, $F(x)$, and that this in turn can be solved for x. A random number $\{R \mid a \leq R \leq b\}$ is drawn and $F(x) = R$ is solved for x (Figure 1.1).

The rejection method on the other hand is always possible to use, but may be very ineffective if the pdf is far from constant. For each sample, two random numbers, R_x and R_y, are drawn. If the coordinate (R_x, R_y) is under the pdf-curve, R_x is an approved sample (Figure 1.2). If not, the process must be repeated.

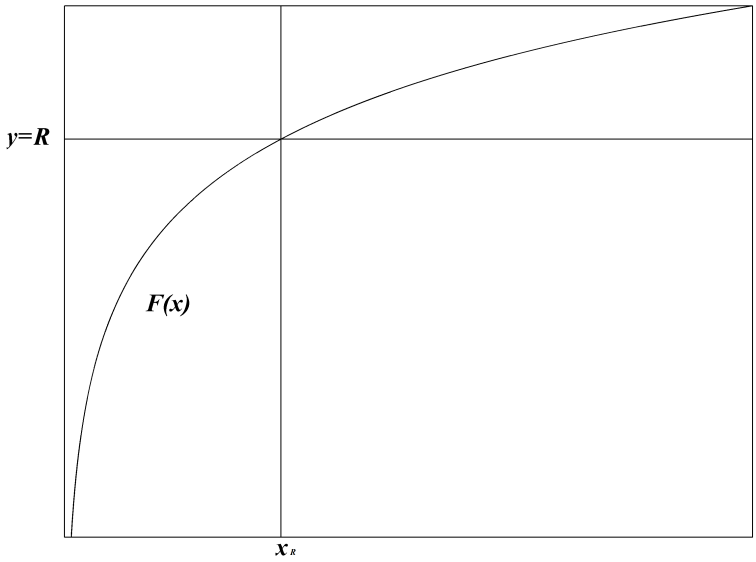

FIGURE 1.1: Inverse transform method. A random number, R (horizontal line), is drawn and set equal to $F(x)$, which is solved for x (vertical line).

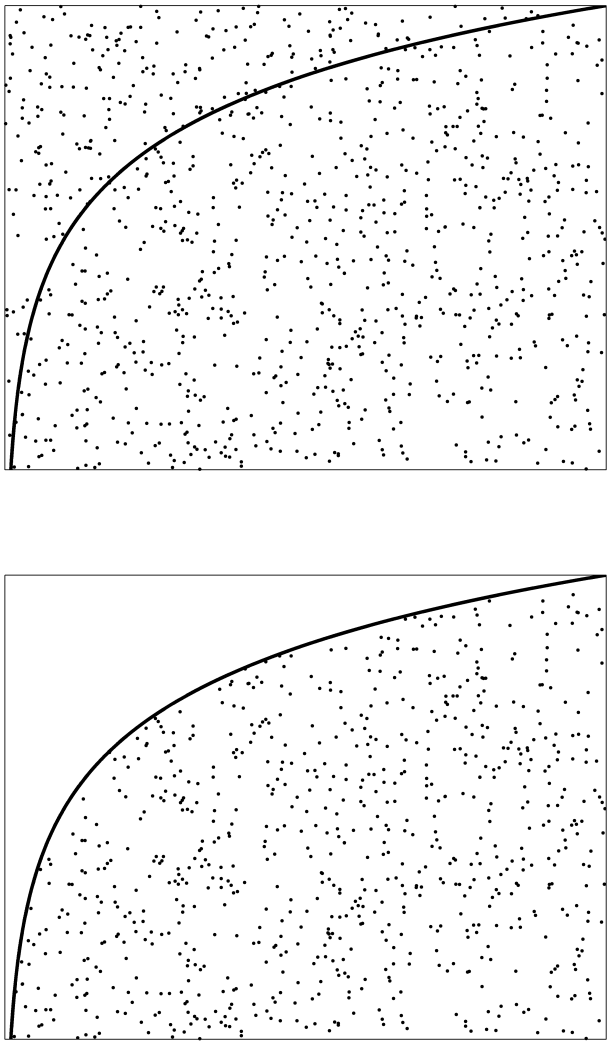

FIGURE 1.2: Rejection method. *Upper panel:* Random coordinates, $(R_{x,i}, R_{y,i})$, are drawn. *Lower panel:* $R_{x,i}$ are accepted samples if ,$R_{y,i} \leq \text{pdf}(R_x)$.

1.6 Green's functions, kernels and convolutions

Bethink the partial differential equation $Lu(x) = f(x)$, where L is a linear differential operator. One way of solving this is to find the inverse operator, L^{-1}, so that $u(x) = L^{-1}f(x)$. Let there be a function, G such that $L^{-1}f(x) = \int G(x,y)f(y)\,dy$, then this function is the Green's function of the operator L or the fundamental solution of the differential equation.

If the operator L is translation invariant, that is independent of x, then G can be considered the impulse response function of the dynamic system, which means that it describes how the system reacts to a small disturbance in one point (such as a δ-function). G may then also be used as a convolution kernel, in convolutions, obviously:

$$\big(f * g\big) \stackrel{\text{def}}{=} \int_{-\infty}^{\infty} f(\xi)\, g(x-\xi)\, d\xi. \tag{1.8}$$

This essentially means moving the function g through every point, calculating the product of f and g everywhere and superposing the results. This process is commutative and either f or g may be considered the kernel. The Green's function for the diffusion equation (Equation 1.4) is the Gaußian (Equation 1.5). This provides that the concentration after any time of a substance diffusing from a point source is described by the Gaußian and that the change in time and space of a volumetric distribution can be calculated by convolving the distribution with the appropriate Gaußian kernel.[24–26]

Another application of convolutions, used in radiation physics, is dose calculation with dose kernels, mainly point dose kernels. This is an indirect Monte Carlo method. A dose distribution is rendered using Monte Carlo for one particular particle (often electrons) in one particular element or compound (often water) and the impulse response, in this case average volumetric dose distribution per emitted particle, is recorded and stored as a kernel that can be used to quickly generate accurate dose results in similar situations by convolving it with for example distributions of cumulated activity, weighted by number of emitted particles per decay.

A typical situation is the convolution of two finite three-dimensional matrices (called matrix and kernel). The desired spatial resolution and dimensions then determine the number of elements in the matrices. A doubling in length causes an 8-fold increase in the number of elements of the matrix and a doubling in spatial resolution

causing an 8-fold increase in size of both the matrix and kernel and since calculations are performed individually for every combination of matrix and kernel element, this leads to a tremendous increase in the required number of calculation steps and thereby time. For this reason convolutions are preferably made with rather small matrices or at least kernels. Fortunately, according to the convolution theorem, a convolution in the spatial domain is the equivalent of multiplication in the frequency domain. Therefore it is possible to calculate the fourier transform (in all three dimensions) of the matrix and kernel, multiply the resulting matrices elementwise and then calculate the inverse fourier transform. If the matrices are sufficiently large the time saved on the calculations exceeds the time spent on transforms. Mathematically , the expression looks like

$$f * g = \mathscr{F}^{-1}\big(\mathscr{F}(f) \cdot \mathscr{F}(g)\big), \tag{1.9}$$

where $\mathscr{F}$ and $\mathscr{F}^{-1}$ are the fourier transform operator respective the inverse fourier transform operator. When working with matrices, that is finite data sets, however it is not possible to calculate continuous fourier transforms, but one has to switch to the discrete version, or the digital analogue if you will. In this form, the general expressions for $\mathscr{F}$ and $\mathscr{F}^{-1}$ become

$$\mathscr{F}\big(f(k)\big) = F(n) = \sum_{k=0}^{N-1} f(k) \cdot e^{-i\frac{2\pi}{N}nk} \tag{1.10}$$

and

$$\mathscr{F}^{-1}\big(F(n)\big) = f(k) = \frac{1}{N}\sum_{n=0}^{N-1} F(n) \cdot e^{+i\frac{2\pi}{N}nk}, \tag{1.11}$$

where $F(n)$ is the fourier transform of $f(k)$ and N is the number of available data points. The fourier transform is based on the fact that all functions can be expressed as a sum of many periodic functions, such as sines and cosines. The result of a discrete fourier transform of a set(N) of real numbers(k) is a set(N) of complex numbers(n) that carry information about the amplitude and phase of the periodic functions that sum up to the original data. The required frequency and phase information only needs $\frac{N}{2}$ numbers, but as a result of the fourier transform, every frequency is generated in pairs, one positive and one negative frequency. Due to some redundant calculations in equations 1.10 and 1.11, it is possible to make clever algorithms that for example omit some steps and can save a considerable amount of time for large sets of data. These algorithms are commonly known as fast fourier transforms(FFT).

Further increase in time efficiency may be achieved by splitting the data into subsets and perform parallel calculations on separate cores or processors.[27]

One consequence of the discretisation, or rather of not including an infinite number of frequencies, is aliasing or folding artifacts. This means that frequency components in the data, higher than the cut-off frequency are interpreted as low frequencies, that are "folded over" on the low end of the frequency span. This effect presents itself in fourier transform-based convolutions as a spill-over of data from one end of the matrix to the opposite and vice versa. In practical use, a way to get around this is to either pad the matrix with nonsense data (preferably minimising the gradients) or simply be aware that data near the edges may not be valid.

Chapter 2

Aim

The aims of this work were

- to characterise the distribution of oxygen in a tumour, by finding the probability density function best suited to describe it and to use this information to model alterations in the distribution to simulate anti-angiogenic therapy in order to quantify the effect of combining this treatment with radionuclide therapy,
- to simulate the effect of modifying the oxygen content of the blood in terms of Hb value and to evaluate in which vascular contexts this may be beneficial for radiation treatment,
- to evaluate the influence on estimated radiation therapy outcome of including longitudinal oxygen variations along vessels, due to oxygen consumption and
- to include variations of the input variables in tumour oxygenation modelling and to investigate the effect of hypothetical correlations between these variables by utilising a novel Monte Carlo approach.

Chapter 3

Methods

This section explains merely the methods that I have used in the four papers. Methods, concerning tissue preparation, used by my co-authors are omitted, but described in paper II. Trivial or self-evident calculations are also excluded from this section. I try to keep a streamlined approach, focusing on the essence of the methods. Methods used several times are described jointly with reference to their applications in the papers, where they are found in context. The reader is assumed to be acquainted with the terms and concepts of the introduction (Chapter 1).

3.1 Characterising oxygen distributions

The previously published experimental data (I, Figure 1) showing the distribution of pO_2 in a tumour before and after antiangiogenic treatment,[20] was fitted by log-normal distributions, that is a distribution whose logarithm is normally distributed. The agreements of the fits are best viewed through cumulative summation (I, Figure 2). The root mean square deviations, RMSD and correlation coefficient, R^2 (r^2), were compared for the assumed distribution and the best normal distribution fit, to ensure that log-normal fit was the appropriate choice (I, Table 1). A third, fully oxygenated, fictive scenario was added, following the same type of distribution, but shifted toward higher values (Figure 3.1).[28] Table 3.1 shows the mean (μ) standard deviation (σ) of the logarithms of the distributions.

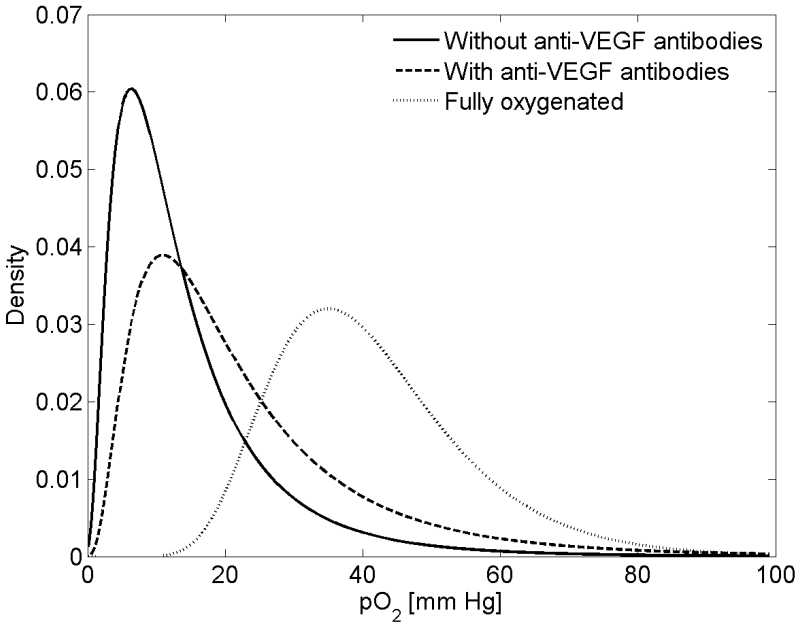

FIGURE 3.1: pO_2 distribution with and without anti-VEGF treatment, as well as a fully oxygenated case, fitted by log-normal distributions. Reprinted with permission from the American Association of Physicists in Medicine.

TABLE 3.1: Parameters of the fitted distributions.

Distribution	μ	σ
Untreated	2.483	0.711
Anti-VEGF treated	2.946	0.689
Fully oxygenated	3.689	0.330

3.2 Distributing activity and oxygen in a spherical tumour model

Oxygen according to the three distributions of section 3.1 was spatially spread out in a spherical 10 g tumour (10^{10} cells, radius 1.34 cm) following two different patterns: One randomised (Monte Carlo) and one radially increasing towards tumour surface. The cumulated activity of ^{90}Y, ^{131}I, ^{177}Lu, and ^{211}At followed the same relative distribution as the oxygen, but the levels of the activity were adjusted (brute force) to give D_{99}.

In the randomised scenario, the distributions (discretised) are sampled radially along voxels of the tumour using the rejection method (Section 1.5) with the additional restraint that the frequency of the selected value must be sufficient to fill the entire shell (10 μm thick) of the tumour represented by the current voxel. This means that spherical symmetry was assumed in order to strongly reduce simulation times.

In the radially depending scenario, the tumour was "filled up" from the outside in going from higher to lower values of the distribution. The values were used in as many shells as required to best represent the frequency of the distribution.

3.3 Calculating oxygen enhancement ratios

The distributions of oxygen enhancement ratios used in I,II,III and IV, have been calculated using the following formula:[29]

$$OER = 1 + \frac{0.81 \cdot \left(pO_2\right)^{0.616}}{1 + 0.324 \cdot \left(pO_2\right)^{0.616}} \tag{3.1}$$

where pO_2 is the distribution of oxygen partial pressure.

3.4 Calculating absorbed dose from cumulated activity distribution

The spatial cumulated activity distributions of section 3.2 were collapsed to a column or "drill core", from the surface to the centre of the tumour. This column was padded on all sides with surrounding voxels from the tumour setup. The thickness of the padding exceeded the range of the emitted particles from the simulated nuclides. This ensured that the column was "unaware" of having been extracted from the complete tumour model. The padded column matrix was convolved with beta point dose kernels,[30] scaled and sampled to fit the nuclides and voxel size, for ^{90}Y, ^{131}I and ^{177}Lu. For ^{211}At, an alpha point dose kernel was used, made from stopping power data.[31] OER (equation 3.1, only for the β-emitters) and TCP (equation 3.2) were calculated. The cumulated activity distribution was scaled and the calculations repeated until D_{99} was found.

3.5 Estimating response to irradiation

Based on the LQ-model, TCP was calculated using a special version of equation 1.3 in II, III and IV, since the oxygen level of the tumours was not homogeneous and in I, neither was the absorbed dose. The expression used was[32]

$$TCP = \prod_{i=1}^{N} \left(1 - e^{-\left(\alpha(OER_i \cdot D_i) + \beta(OER_i \cdot D_i)^2\right)}\right), \tag{3.2}$$

where OER_i and D_i were the individual (cell by cell) values of OER and D and N was the total number of cells in the tumour. α and β were the radiation sensitivity parameters of the LQ-model and their values are presented in Table 3.2. The parameter values are not critical, but have been selected within reasonable limits to give clinically relevant D_{99} values.[33]

TABLE 3.2: Radiation sensitivity parameters used in the calculations.

Paper	α $\left(\text{Gy}^{-1}\right)$	β $\left(\text{Gy}^{-2}\right)$
I	0.35	0
II	0.01	0.001
III	0.01	0.001
IV	0.02	0.002

TCP was calculated iteratively until D_{99} was found.

3.6 Building an expandable 3D vessel distribution module

Tissue samples of insulinoma from mice were immunostained, sliced and photographed by my co-authors Eliane Cortez and Kristian Pietras, at the time operating at Karolinska Institutet.

Using the microscopy images of 12 μm thick serial slices of tumour tissue[34] (n = 14) with green coloured vessels, binary images of the vessels were created by thresholding the images (II, Figure 1).

These images were aligned by translation and rotation for maximum visual and numerical agreement; two adjacent binary slice images were combined with a third dummy-layer of zeros to form a three-layer matrix the size of the image. The matrix was then displayed as an RGB-image, where the two binary images represented the red and blue layers respectively and pixels corresponding to matrix ones in both layers therefore became magenta colored. This was used as a visual tool for measuring overlap.

The matrix layers were also multiplied element-wise and the sum of the resulting product matrix was divided by the lowest of the sums of the two layers. The result

was a numerical measure of the vessel overlap between the two layers where 0 means no overlap and 1 means full overlap. The aligned stack of images was then cropped to form a 3D image entirely representing the tumour tissue.

Individual vessels were separated through segmentation. Vessel voxels were considered part of the same vessel if they belonged to the same 26-connected neighborhood. All vessels were individually identified and labelled and every vessel not connected to at least two vertices of the 3D matrix was rejected in order to avoid using dysfunctional vessels in the calculations. The images were down-sampled to cubic voxels with all sides equal to slice thickness.

In order to negate the influence of a lack of oxygenation around the edges of the sample, the 3D image matrix was enlarged by mirroring in all directions and concatenation into a cube twice the original matrix size in each direction. This approach created an expandable module that could be extended in any direction and to any size without losing vessel continuity.

3.7 Simulating altered vessel density and oxygen tension

The expandable 3D vessel distribution module from the previous section was expanded to a 2x2x2 mm^3 cube of tumour tissue which was then used to simulate oxygenation, assuming a constant vessel pO_2 of 40 mmHg. Various cases of diffusion-limited hypoxia were simulated by randomly reducing the fraction of vessels in the tumour matrix. This was possible since the tumour type used is considered highly vascularised. As well the removed as the remaining vessels were entire and connected. The fraction of vessels removed was $10, 20, ..., 90$ %.

The model was also used to simulate anemic hypoxia by altering the vessel pO_2, corresponding to an equal change in Hb concentration from 14 to 7 (50 % decrease), 10.5 (25 % decrease), and 17.5 (25 % increase) g/dl. All 40 combinations of the above parameters were simulated.

3.8 Calculating oxygenation-induced dose amplification

The oxygenation-induced dose amplification (ODA), defined in II, is a relation between Hb concentration and D_{99}. The reference used is D_{99} at Hb concentration 7 g/dl (not 70 mmHg as mistyped in II, page 4) such that

$$ODA(Hb) = \frac{D_{99,ref}}{D_{99}(Hb)}, \tag{3.3}$$

that is a measure of how many times higher absorbed dose is required for TCP=0.99 at the reference Hb concentration compared to the current value. ODA was calculated for each of the 40 scenarios of II.

3.9 Modelling oxygen diffusion

Diffusion was modelled in II, III and IV, using a Green's function approach.[35] A tissue and vessel matrix was convolved with a Gaußian kernel (Equation 1.5). The kernel was scaled with the time step and sampled using the voxel size of the model setup. Table 3.3 shows the parameter settings. The values were selected based on physical properties, such as tissue slice thickness and acceptable simulation times.

TABLE 3.3: Parameters settings used in the diffusion simulations.

Paper	Time-step (s)	Voxel side (μm)	Diffusion coefficient ($\mu m^2 s^{-1}$)
II	0.01	12	2000
III	0.1	10	2000
IV	0.1	10	2000

The convolution was repeated once every time-step and between each step, oxygen consumption was applied and vessel values were adjusted. In II, the oxygen content of the vessels was kept constant at 40 mmHg, while in III and IV, vessel oxygen started high and successively was consumed, whereas the blood was flowing in the vessels, bringing more oxygen into the system. In these cases, the oxygen buffer in the haemoglobin had to be taken into account.

In II, the diffusion simulations were done as described above (Section 3.7).

In III, the blood velocities used were 1500 and 2500 μm/s, the initial vessel oxygen tension was 100 mmHg and the vascular fraction was varied between 0.02 and 0.12. Two scenarios, constant and variable vascular fraction, were compared against a reference scenario with constant vessel pO_2 of 40 mmHg. The simulations were done for parallel vessels entering the tissue in one end, in order to create a depth oxygenation curve (DOC) and the corresponding oxygen gradients for use in further simulations (Section 3.12).[36]

The simulations in IV were done on all 27 combinations of the parameters in table 3.4. These results were then fitted to analytical expressions and used in simulations (Section 3.14).

TABLE 3.4: Parameters simulated in IV.

Vessel pO_2 mmHg	Blood velocity (μms^{-1})	Vascular fraction
60	1500	0.0400
80	2000	0.0625
100	2500	0.1111

3.10 Modelling oxygen consumption

Oxygen consumption in II, III and IV was simulated using the Michaelis-Menten kinetics model, which is very widely used as a better alternative to constant consumption,

$$C = \frac{C_0 \cdot pO_2}{pO_2 + K_M}, \tag{3.4}$$

where C is oxygen consumption per unit volume of tissue, C_0 is the oxygen consumption at unlimited supply and K_M is the Michaelis constant, that is the oxygen partial pressure at which $C = 0.5 \cdot C_0$.[37] In these studies, $C_0 = 15$ mmHg/s[36,38,39] and $K_M = 1$ mmHg.[35] This means that when oxygen is low, the cells consume less. The total consumption is calculated per time-step for each voxel and subtracted from the volumetric tissue oxygen distribution at every step.

3.11 Calculating haemoglobin saturation

In III and IV, where vessel pO_2 was dynamic, haemoglobin saturation had to be calculated. The haemoglobin saturation curve used is based on the Hill equation with corrections for increased validity (Figure 3.2). The data describes the ratio of bound oxygen to the carrying capacity of the haemoglobin as a function of blood pO_2.[40] At every simulation step, the total amount of oxygen (bound and solved) in the blood was calculated according to equation 3.5

$$O_{2,total} = 1.34 \cdot \mathrm{Hb} \cdot 0.01 \cdot S + 0.000031 \cdot \mathrm{pO}_2, \tag{3.5}$$

where $O_{2,total}$ is the total volumetric fraction of oxygen in the blood at standard pressure, 1.34 ml/g is the oxygen carrying capacity of haemoglobin, Hb is the haemoglobin concentration (g/dl), 0.01 is dl/ml, S is the saturation and 0.000031 mmHg^{-1} is the solubility coefficient of oxygen in plasma.[11]

The pO_2 of the vessel before and after diffusion convolution (Section 3.9) were compared and the difference was subtracted from the value of total amount of oxygen in the vessel voxels. The resulting oxygen amount was then redistributed between bound and solved using equation 3.5 and the saturation curve. These calculations were done voxel by voxel. The saturation curve is slightly affected by parameters such as pH, temperature and concentrations of CO and CO_2. These variations are beyond the scope of this study.

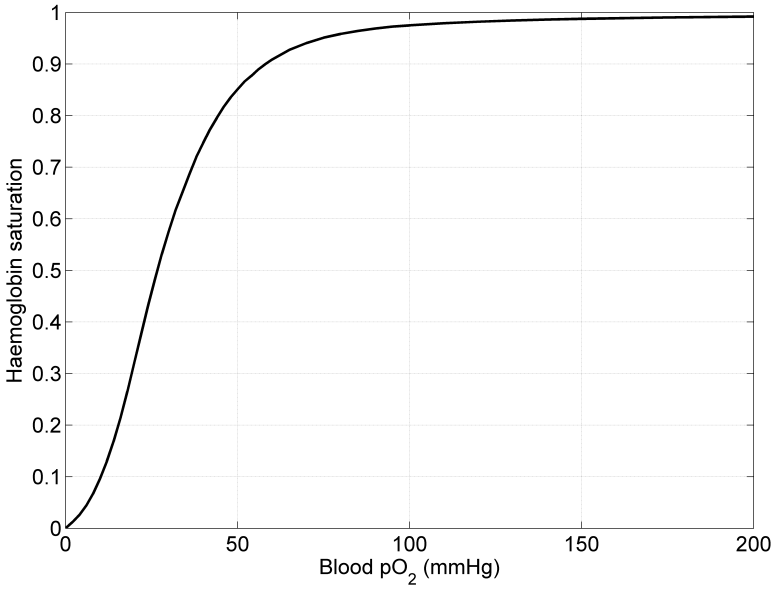

FIGURE 3.2: Haemoglobin saturation vs. pO_2 of the blood.

3.12 Modelling oxygenation in spherical tumours

Spherical tumour models in III were constructed of 10x10x10 $\mu\mathrm{m}^3$ cubic voxels to create a total mass of 1, 10, 100, 1000 and 10000 mg, which corresponded to 10^6, 10^7, 10^8, 10^9, and 10^{10} tumour cells. Vascular fraction was set at the surface of the tumour.

Surface VF was varied between 0.02 and 0.12. Three scenarios of variation of vessel oxygen pressure and vascular fraction were examined:

CVO The simplest scenario, using constant vascular fraction and **c**onstant **v**essel **o**xygen levels with a blood pO_2 of 40 mmHg in the vessels, a common value used in models.

CVF The more advanced scenario with **c**onstant **v**ascular **f**raction and longitudinally (spatially) variable vessel oxygen levels.

VVF The most advanced scenario with **v**ariable **v**ascular **f**raction and longitudinally variable vessel oxygen levels. This is to evaluate whether it is plausible that the longitudinal decrease of vessel oxygen content could be compensated for by an (hypoxia driven) increase in VF along the vessel. In this scenario, VF increased along the vessel direction (towards tumour centre), proportional to the square of the distance from tumour surface, to a maximum of 0.22 (corresponding to an vessel spacing of about 21 μm) and thereafter remained constant to avoid physiologically unreasonable vessel spacing.

The DOC and gradient curves generated in the simulations described in section 3.9 were used for the simulations. The surface value was determined from the DOC curve and the gradients were used as a lookup table to determine the radial oxygen difference, voxel by voxel, depending on the vessel spacing. This information was then used to calculate the pO_2 profile of the tumour, according to equation 3.6:

$$O_i = r_i^2 \left(O_{i-1} + (r_i - r_{i-1}) \cdot \frac{\partial O}{\partial r_{vd_i,O_i}} \right) \tag{3.6}$$

where O_i is the pO_2 value of the i:th voxel, r_i is the radial position of that voxel, and vd_i is the vessel spacing.

Assuming spherical symmetry, each voxel value along this profile line was weighted based on its distance from tumour centre so that it represented all voxels in the sphere on the same radial position to form homogeneous spherical layers. This was to create a distribution of oxygen that represented the entire sphere. We also calculated the necrotic fraction, which we defined as the regions where the pO_2 value fell below 1 mmHg.

3.13 Verifying vascular heterogeneity

The RCC image used in IV (Figure 1 a of IV) was transformed from Cartesian to polar coordinates, with the centre of the necrotic core as reference point and samples of pixel value histograms were collected along horizontal (angular direction) and vertical (radial direction) profiles (Figure 3.3). Because the circumference varies with radius, the distance between points in the transformed image appear stretched in the angular direction. This, however, does not distort the shape of the pixel value histograms. High pixel values indicate high contrast uptake, likely to be part of a vessel, the higher value, the larger vessel, whereas the width of the distribution is a measure of the heterogeneity of size. From the image itself and from the difference in shape between the histograms it is obvious, however, that the vascular intensity of the tumour varies with angle and radius. Therefore it is likely that the oxygenational status of tumours varies with position. This is rationale for the modelling of varying pO_2 of incoming blood, blood velocity and vessel spacing.

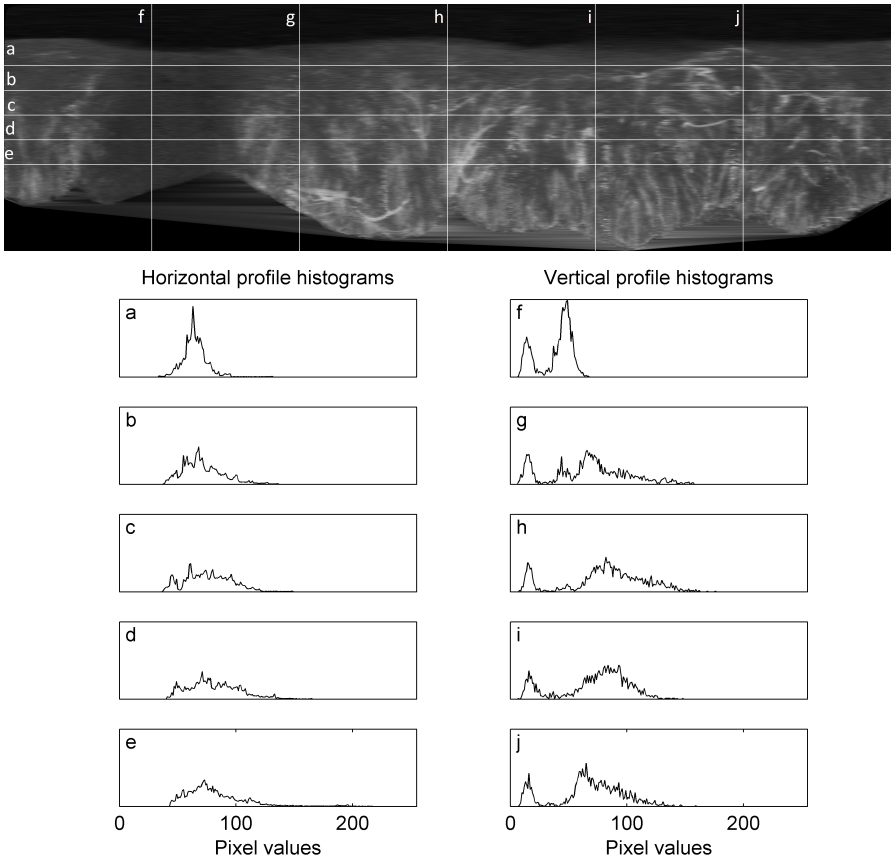

FIGURE 3.3: RCC angiogram in polar coordinates, with radius vertically and angle horizontally. The centre point of the necrotic core in the original image corresponds to the top of the image and the angle starts and ends between the second and third quadrant (i.e. on the negative x-axis) and the direction from left to right is clockwise. The histogram curves on the left hand side (a through e) correspond to the horizontal profile lines and those on the right hand (f through j) represent the vertical profile lines from left to right.

3.14 Modelling vascular and oxygenational heterogeneity

In IV, a spherical tumour was inscribed in a cube. A coordinate $P = (x, y, z)$ was randomly selected within the cube. If P is inside the tumour, the shortest distance between P and the tumour surface was calculated.

This model was used to compare the oxygen distribution from the primary DOC (referred to as the ideal or "no variation" scenario), to six other oxygen distributions generated by randomised selection of initial blood pO_2, blood velocity (BV) and vessel proximity (VP), with and without correlation between the variables, for tumour radii of 5, 10, 20 and 30 mm. Vessel proximity was here defined as a conceptually inverted numerical equivalent to vessel distance. This circumlocution was used to give an intuitive understanding of the correlations. Table 3.5 shows the correlation conditions of the six scenarios. The correlations are perfect, that is $R^2 = 1$ or -1. This means that the parameters were selected from the same (or mirrored) positions of their respective distribution, in terms of mean value and standard deviation.

TABLE 3.5: Correlations between vessel pO_2, blood velocity and vessel proximity in the different scenarios. 1 and 1 means correlation coefficient $R^2 = 1$, 1 and -1 means correlation coefficient $R^2 = -1$, while 0 means uncorrelated parameter.

Scenario	pO_2	BV	VP
1	0	0	0
2	1	1	0
3	1	0	1
4	0	1	1
5	1	1	1
6	No variation		
7	1	0	-1

Oxygen profile functions for interpolation were selected by sampling from three Gaußian distributions specified in table 3.6, where all distributions were truncated at ±2 SD. The oxygen level of P was then determined by interpolation between the selected functions for the distance between P and the tumour surface. An oxygen distribution was constructed from 10000 point values.

TABLE 3.6: Mean (μ) and standard deviation (σ) for the normal distributions of pO_2, blood velocity and vessel proximity used in the simulations.

Variable		μ	σ
pO_2	(mmHg)	80	10
BV	(μm/s)	2000	250
VP	(μm)	40	5

Chapter 4

Results

4.1 Combining antiangiogenic treatment with radionuclides

The oxygen distributions in I, are best described by a log-normal distribution, both in terms of coefficient of determination (R^2) and root mean square deviation (RMSD). For comparison, Table 4.1 shows goodness of fit for normal and log-normal distributions. The three log-normal distributions (untreated, anti-VEGF treated and fully oxygenated) are shown in Figure 3.1.

TABLE 4.1: R^2 and RMSD from cumulative sum of oxygen distribution fit for anti-VEGF treated and untreated tumour.

	Normal distribution		Log-normal distribution	
Case	R^2	RMSD*	R^2	RMSD
Untreated	0.979	0.038	0.997	0.017
Anti-VEGF treated	0.931	0.078	0.996	0.019

*) Root mean square deviation: The mean of the squared deviation between each model prediction and the corresponding data point.

The absolute D_{99} values are highly dependent of the number of tumour cells (tumour size) and the chosen radiation sensitivity (α and β), since the TCP is the product of the probabilities of killing each single tumour cell (Eq. 3.2), whereas the relative differences in D_{99} due to oxygen enhancement are independent of tumour size and radiation sensitivity. Therefore this is an interesting measure.

Since the distribution of radionuclides depends on e.g. perfusion of the tumour tissue and due to the limited particle range, their dose distributions may be highly nonuniform. Right-shifted oxygen distributions cause left shifted D_{99} values. In the

fully oxygenated scenario with homogeneous irradiation, the absorbed dose reduction is as high as 33% compared to the untreated case, while in some of the radionuclide comparisons, the relative decreases are as high as 96 per cent. For the complete result, se table 4.2. All absorbed doses are relative to untreated case with radially dependent distribution.

TABLE 4.2: Average reduction in D_{99}, for each radionuclide and for homogeneous irradiation, relative to untreated case with radially dependent distribution.

		^{90}Y	^{131}I	^{177}Lu	^{211}At	Homogeneous
Radial distribution	Untreated	0.00	0.00	0.00	0.00	0.00
	Anti-VEGF treated	0.35	0.28	0.35	0.19	0.08
	Fully oxygenated	0.86	0.92	0.92	0.82	0.33
Random distribution	Untreated	0.75	0.71	0.76	0.53	0.00
	Anti-VEGF treated	0.79	0.75	0.82	0.65	0.08
	Fully oxygenated	0.93	0.96	0.96	0.93	0.33

It is obvious that the required absorbed doses are lower in the case of randomly distributed activity and oxygen tension than in the radially dependent scenario. This is due to cross dosage from hot areas, compensating for lower activity in colder areas within range. Further it can be noticed that the difference between random and radially dependent distributions decrease with antiangiogenic treatment. This is because the tumour response is highly influenced by cold spots. Because the effect of α-emitters is very local compared to electron emitters due to lack of cross irradiation and because of the absence of oxygen enhancement and dose distribution synergetics, the intratumoural dose variations remain bigger and the D_{99} reduction is more modest.

4.2 Modification of blood oxygenation – effects on radiation response

The results from the simulations in II show that as the vessel density decreased, the oxygen distribution broadened and shifted to the left, showing a log-normal distinction, while the result of decreased pO_2 of the blood appeared to be a shift to the left of the entire original distribution in which there was no pronounced log-normality. The combined scenarios caused left-shifted, narrow distributions with explicit log-normal characteristics. In the cases where 50% vessel reduction was combined with a 25% increase in blood pO_2 (Figure 4.1 H), the distribution was centered at about the same value as in the reference case (Figure 4.1 C), only wider, due to the lack of

vessels. A selection of distributions are shown in Figure 4.1. Figure 4 of paper II adds information on the spatial distribution.

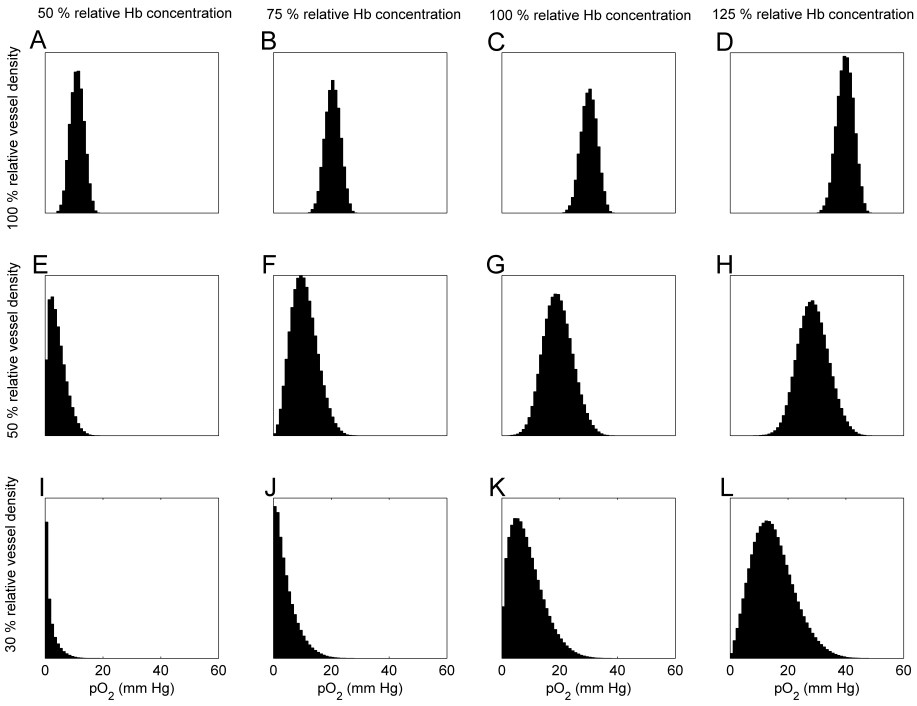

FIGURE 4.1: Simulated pO_2 histograms. Abscissa: 50%, 75%, 100%, and 125% of relative Hb concentration. Ordinate: 30%, 50%, and 100% of relative vessel density. Permission obtained from the American Association of Physicists in Medicine.

Figure 4.2 presents the results from the D_{99} calculations. The influence of a 50% decrease in blood pO_2 on the required absorbed dose was slightly higher than that of an equal decrease in vessel density when both were compared to the reference case (100% vessel density). This result is due to the oxygen distribution in the former case being shifted further to the left but still narrow, which puts a major part of the distribution in the pO_2 region where OER is low (Equation 3.1). The D_{99} and TCP values for the scenarios with increased pO_2 and decreased vessel density were rather similar to those of the reference case, as the means were similar but the distribution width at such high values had a limited effect on the OER values.

Figure 4.3 shows the corresponding ODA values.

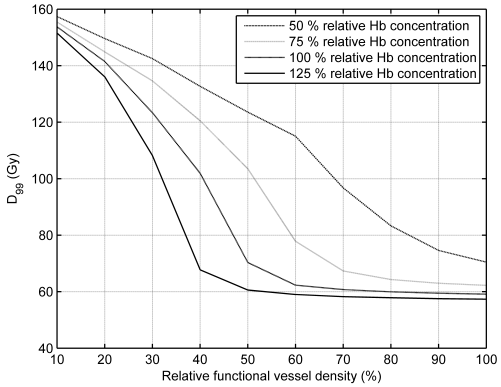

FIGURE 4.2: D_{99} for various combinations of relative Hb concentration and relative functional vessel density. Solid, dashed, dotted, and dashed-dotted lines represent 125%, 100%, 75%, and 50% relative Hb concentration, respectively. Permission obtained from the American Association of Physicists in Medicine.

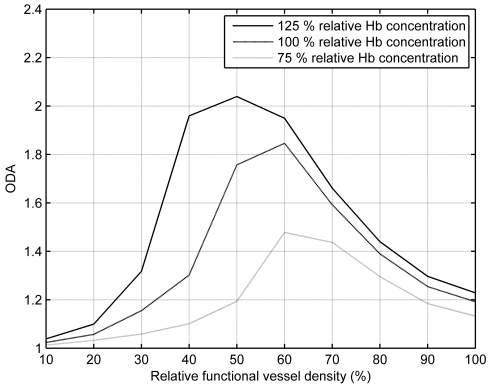

FIGURE 4.3: The oxygen-induced dose amplification (ODA) curves for different relative Hb concentrations as a function of relative functional vessel density. Solid, dashed, and dotted lines represent 75%, 100%, and 125% relative Hb concentration, respectively. Permission obtained from the American Association of Physicists in Medicine.

4.3 Oxygen variations along vessels – effects on radiation response

Constant Vessel Oxygen

D_{99} values for tumour masses from 1 mg to 10 g in the CVO scenario of III, were determined through simulations with a constant oxygen content of 40 mmHg in the blood vessels. We found that large vascular fractions could reduce the D_{99} by up to 10%, and that the D_{99} vs. vascular fraction dependence is similar for the different tumour masses (Figure 4.4). In the this scenario, the necrotic fractions are 0, even for large tumours.

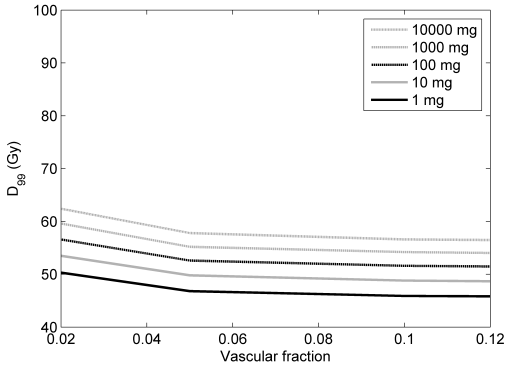

FIGURE 4.4: D_{99} values from the CVO model
for tumor sizes from 1 to 10000 mg. Permission obtained from the American Association of Physicists in Medicine.

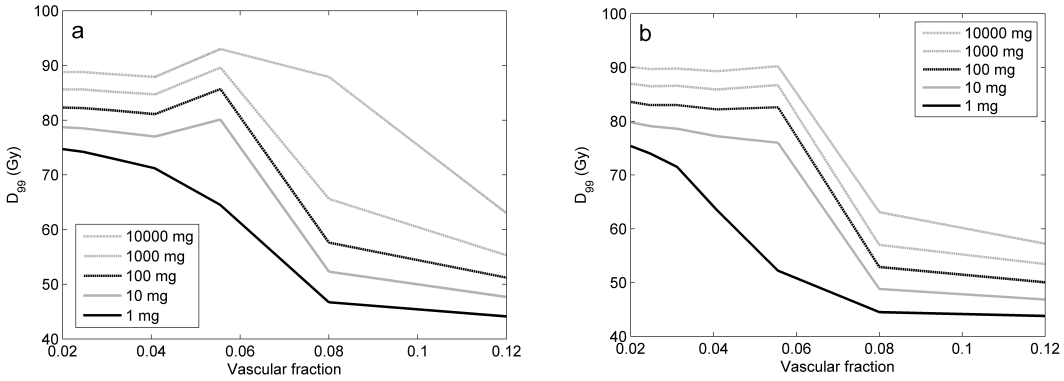

FIGURE 4.5: D_{99} values from the CVF model for tumor sizes from 1 to 10000 mg.
(a) Blood velocity: 1500 μm/s. (b) Blood velocity: 2500 μm/s. Permission obtained from the American Association of Physicists in Medicine.

Constant Vascular Fraction

In the more realistic CVF scenario, variable vessel oxygen due to consumption was included in the model, which generates a continual decrease in oxygen content along the blood vessel. This model demonstrates a clear difference from the CVO model. There is a modest effect on D_{99} of increased blood velocity, 2500 μm/s compared to 1500 μm/s (Figure 4.5). This is most evident in the 10 g tumour of the CVF scenario. Corresponding necrotic fractions are shown in Figure 4.6.

Variable Vascular Fraction

Generally, the differences between CVF and VVF scenarios are minor. When comparing blood velocities, we found that D_{99} tends to decrease with increasing blood velocity and that this appears less size dependent in the VVF than in the CVF scenario (Figures 4.5 and 4.7). For all tumour sizes, the necrotic fraction decreases with

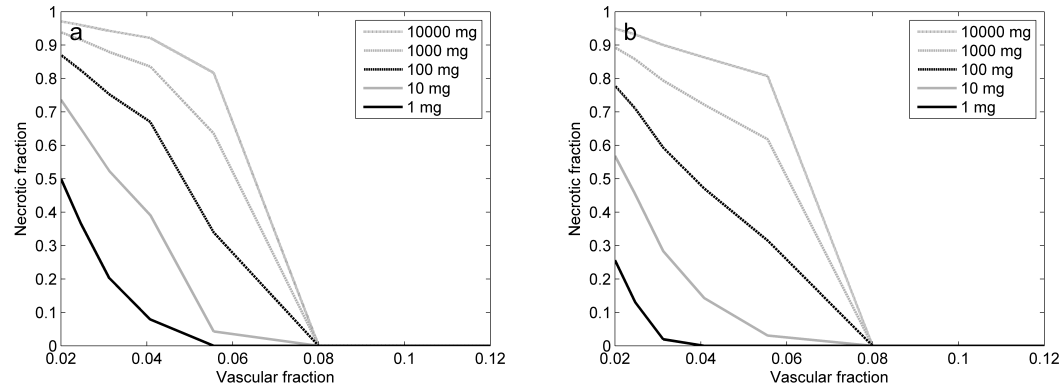

FIGURE 4.6: Necrotic fractions from the CVF model for tumor sizes from 1 to 10000 mg.
(a) Blood velocity: 1500 μm/s. (b) Blood velocity: 2500 μm/s. Permission obtained from the American Association of Physicists in Medicine.

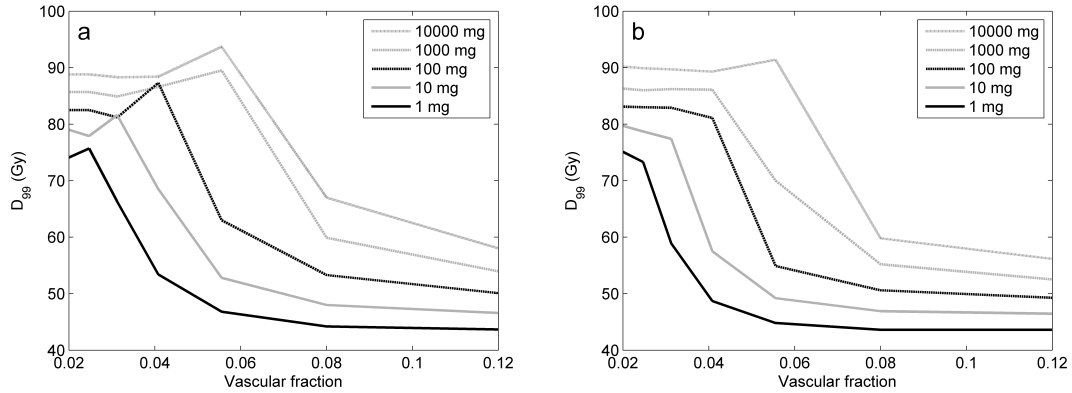

FIGURE 4.7: D_{99} values from the VVF model for tumor sizes from 1 to 10000 mg.
(a) Blood velocity: 1500 μm/s. (b) Blood velocity: 2500 μm/s. Permission obtained from the American Association of Physicists in Medicine.

increasing blood flow. This effect is best observed at low vascular fractions. There is a clear difference between the CVF and VVF scenarios in the sense that the necrotic fractions of small tumours decrease more with increased vascular fraction in the VVF scenario. The same tendency of difference in oxygenation also shows clearly in the D_{99} where for example the value for the 1 mg tumour at VF= 0.04 drops from about 70 Gy to about 55 Gy between the CVF and VVF scenarios. Necrotic fractions for VVF scenario are shown in Figure 4.8.

General observations

The vascular fraction provides the most profound influences, for the VVF as well as the CVF scenarios, on the D_{99} and the necrotic fraction, slightly stronger on smaller tumours. The results show that an increased vascular fraction could eliminate the necrotic fractions in all tumours sizes tested, but the necrotic parts of the larger

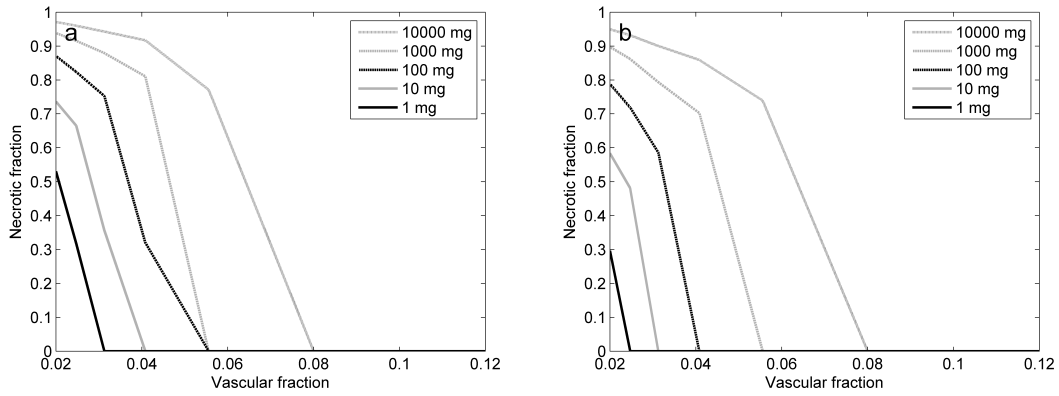

FIGURE 4.8: Necrotic fractions from the VVF model for tumor sizes from 1 to 10000 mg. (a) Blood velocity: 1500 μm/s. (b) Blood velocity: 2500 μm/s. Permission obtained from the American Association of Physicists in Medicine.

tumours (i.e. the 1 and 10 g tumours) are considerably persistent compared to smaller tumours. Where there are large necrotic regions in the tumours we can observe some fluctuations in D_{99} values vs. vascular fraction. Where these regions disappear, at higher VF, the D_{99} values tend to stabilise. At high vascular fractions (above 0.12), the difference in D_{99} values between all scenarios becomes less evident.

4.4 Correlation between variables in tumour oxygenation models

From Figure 4.9 we can see that the shape of most of the distributions sampled from varying depth oxygenation curves, with exception of corr(pO_2, vessel proximity)=-1 (scenario 7) are quite different from the ideal curve (scenario 6), and also more similar to oxygen distributions measured in vivo, with a normal or log-normal profile.

The shape of the six distribution based curves and the no variation scenario vary between themselves and appear to be more or less divided into three groups: a) scenarios 1,2 and 4; b) scenarios 3 and 5; c) scenario 6 and 7, referring to the nomenclature used in section 3.14. This is most clearly visible in the cumulative pO_2 distributions in Figure 4.9 b and d. Because of this observation, the further analysis was focused on scenarios 1, uncorrelated parameters (UP); 3, vessel proximity oxygen positive covariance (PVO+C); 6, Depth oxygenation curve (DOC) and 7, vessel proximity oxygen negative covariance (VPO-C). Figures 4.10, 4.11 and 4.12 show the hypoxic fractions, mean oxygen levels and D_{99} values respectively for each distribution as a function of tumour radius.

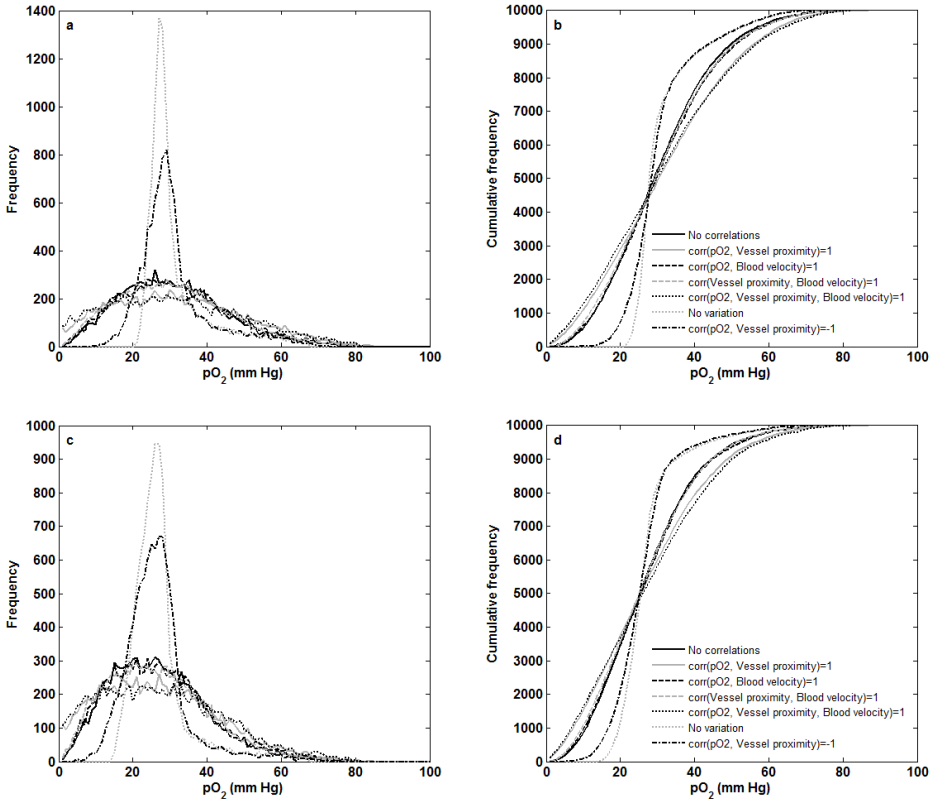

FIGURE 4.9: a) Relative volumetric pO_2 distribution for 5 mm tumour radius, b) cumulative pO_2 distribution for 5 mm tumour radius, c) relative volumetric pO_2 distribution for 30 mm tumour radius and d) cumulative distribution for 30 mm tumour radius.

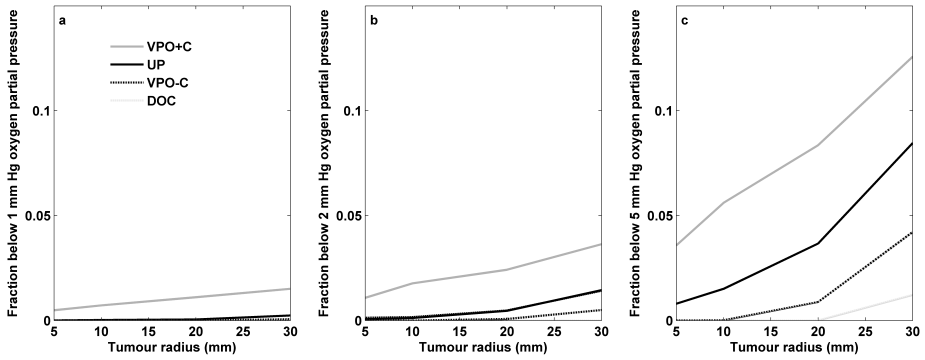

FIGURE 4.10: Fractions of various degree of hypoxia: a) 1 mmHg, b) 2 mmHg, and c) 5 mmHg versus tumour radius for different correlation scenarios.

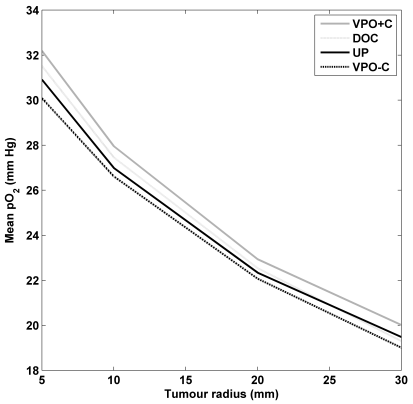

FIGURE 4.11: Mean pO_2 for different distributions for tumour radii 5, 10, 20 and 30 mm.

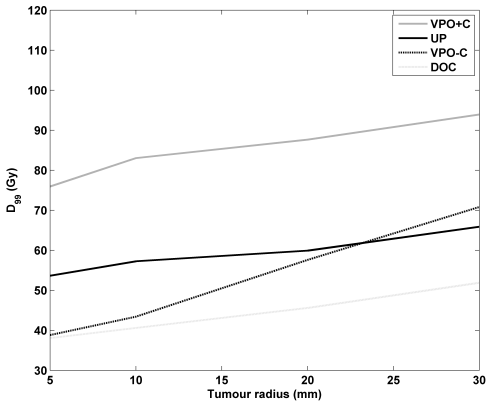

FIGURE 4.12: D_{99} curves versus tumour radius for different correlation scenarios.

Chapter 5

Discussion

5.1 Combining antiangiogenic treatment with radionuclides

Radiation damage to normal tissue is often the limiting factor when it comes to therapeutic dose levels. Consequently this also limits the damages to tumour tissue and thereby the probability of tumour control. An increase in tumour response gives a therapeutic gain without additional damage to normal tissue. Our results show a potential for improving radionuclide therapy by increasing tumour oxygenation and uniformity of activity distributions.

The observed log-normal distribution of oxygen tension in this study may not seem very intuitive at first, although this type of distribution often is observed in in vivo measurements.[41] The log-normal distribution is to multiplicative processes as the normal distribution is to additive and there are physical arguments in support of this type of distribution.[42] Apart from this, there are studies showing that radionuclides tend to distribute log-normally among cells even in vitro, which points at biological causes.[43]

The volumetric distribution of oxygen in the tumour appears to highly affect the results of antiangiogenic treatment, as demonstrated in these simulated scenarios. Because of cross-irradiation, the distribution of the radionuclides is less important the longer the range is. This may lower the required absorbed doses but also cause more normal tissue damage, especially in small tumours. Our modelled scenarios are simplifications; in real treatment situations, it is likely that the distribution of radionuclides differs from the distribution of oxygen since many radiopharmaceuticals target either antigens or receptors, which may distribute differently.

The oxygen distribution of the ideal scenario was centered around 40 mmHg, which is approximately the mean for normal tissues. The distribution shape is not critical here, as replacing it with a δ-function causes a relative shift of the TCP-curve by 0.01, assuming homogeneous absorbed dose. For scenarios with a higher prevalence of low pO_2 values, the distribution shape is of higher importance. In e.g. the untreated scenario, there is a relative TCP shift of 0.07 for the two level model compared to the continuous distribution. This is an example of why the often used hypoxic fraction[44–47] is a poor indicator of oxygen effective dose.[48]

Today, radiopharmaceuticals such as radiolabelled somatostatin analogues,[49] antibodies,[50] and microspheres,[51] show beneficial values for patients – in terms of prolonging life and improving quality of life. Although cure usually is not obtained, there is great potential of improvement in this area. This study exemplifies the synergism that can come from combining radiopharmaceuticals with antiangiogenic drugs, thereby increasing uptake of oxygen as well as radionuclides. The effect is highly dependent on time of administration as there is an optimal time window, due to the temporal effects of the antiangiogenic drugs.[22] Additional factors complicating the issue is for example difference in kinetics between large molecules such as anti-VEGF and small, such as radiopharmaceuticals, which may introduce time shifts, blur the cumulated activity distribution and cause uncertainties in biological half lives.

5.2 Modification of blood oxygenation – effects on radiation response

The log-normal characteristics of the simulated distributions agree with the observations in our previous study (I), in which measured oxygen tension fields were best-fitted by the log-normal distribution. The great variations in distribution shapes emphasise the importance of considering the entire oxygen distribution in OED estimates.

In this three-dimensional approach, every layer of the tumour matrix is unique regarding the blood vessel pattern, which results in a flow of oxygen between tumour layers and an averaging of oxygen levels throughout the tumour, whereas two-dimensional models describe one single tumour layer.[36,52] This is equal to a three-dimensional model where all layers are identical, that is an unrealistic model where all vessels are perfectly parallel and no "cross-talk" of oxygen between layers exists. All changes applied to such a model will therefore effect every layer. This probably results in an

overestimation of the average distance to nearest vessel and thereby of the heterogeneity of the oxygen distribution.

At the interfaces of model modules, there is a mirroring, in order not to lose continuity of vessels. The resulting effect of the similarity of vessel structure on both sides of the border and of the repetitive pattern in the fully vascularised scenarios on the volumetric oxygen distribution in the tissue is negligible.

According to our results, the differences in D_{99} and ODA between different Hb concentrations are quite small for both high and low vascular densities (Figures 4.2 and 4.3). In the intermediate region, however, a considerable difference was found. For example, at 50% relative vessel density, D_{99} is 63 Gy higher, for the least compared to the most favourable Hb concentration. Thus, the ODA at 125% relative Hb concentration equals 2. Because the tumour type (insulinoma) used in this model is densely vascularised, it is a reasonable assumption that many tumours have a vascular density that falls within this intermediate region.

The in vivo material used in the study stems from a genetically engineered mouse model that develops an initially well vascularised tumour (pancreatic neuroendocrine carcinoma/islet cell tumour). Eventually, however, the tumours transform into invasive multifocal carcinomas and become fully comparable to several other preclinical mouse tumour models used in similar studies.[53]

Hypoxia is associated with less favourable treatment results.[54] Further, low Hb concentration is considered an indication of poor tumour oxygenation. Increasing Hb concentration improves overall oxygenation although unnaturally high values are not believed to further strengthen the oxygenational status of tumours but may even have a bad influence.[55] Adjustment of low Hb levels by blood transfusion prior to treatment has not been demonstrated to improve treatment outcome.[56] Erythropoietin treatment of anemic patients in combination with radiotherapy also provides ambiguous results.[57]

5.3 Oxygen variations along vessels – effects on radiation response

The simulation results from the simplified models show no necrosis, regardless of tumour size, and no dependence on either tumour size, or blood velocity unlike the advanced models, which provided that increasing the oxygen flow into a tumour resulted in improved oxygenation. We also found that well-oxygenated tumours are more

radiosensitive than poorly oxygenated tumours and therefore required a lower absorbed dose for sterilisation. This, however, is strictly true only for tumours without necrotic regions.

In the presence of necrosis, however, better oxygenation will not always result in a lowered required absorbed dose. Even though the living cells become more sensitive to radiation, it may be necessary to kill more cells, for equal TCP, due to a smaller necrotic fraction. In a hypothetical, spherical tumour with a necrotic core there would be hypoxia as well and if the tumour were spherically symmetric, the hypoxic region would be shell shaped. Increasing the oxygen tension of such a tumour would cause different behaviour depending on the location of the hypoxic shell. If the hypoxia were close to the surface (typically large tumours), its volume will depend less on the radial location than if it were more centrally located, why increased oxygen penetration depth in the former case would cause less of a shrinkage of the hypoxic region than in the latter case. The normoxic regions would increase and the anoxic would decrease in both cases. The increased radiosensitivity is then more likely to be cancelled by the increased number of living cells in the former case, which in turn would be more likely to occur in a large tumour, while in a small, the shrinking hypoxic region would work together with the increased normoxic region to lower D_{99}. This effect may show up as fluctuations in D_{99} vs. vascular fraction where one expects a strictly rising curve (Figures 4.5 and 4.7). The importance of this effect is also highly dependent of necrosis threshold and therefore very imprecise in the results. In the simulations, it was assumed that all tumour cells became necrotic when the pO_2 fell below 1 mmHg. This assumption is a simplification that may also overestimate radiosensitivity, as some of these cells may be quiescent but alive, and hence, very radioresistant. However, the pO_2 is the best parameter available for modelling necrotic regions, and 1 mmHg appeared to be a reasonable limit. There are different examples available in the literature of values used for hypoxic and necrotic fractions. To our knowledge, no pO_2 level threshold for necrosis induction has been determined.

Administration of absorbed dose at a single exposure as in the simulations is not standard procedure, for various reasons. In the clinical setting, the dose is usually administered during an extended time period, using one of several available modalities. During this time period, cells are cleared from the tumour resulting in decreased overall tissue oxygen consumption, which might improve tissue oxygenation and thereby tumour response. A more clinically relevant estimate of the D_{99}

would require the inclusion of for example proliferation and cell death dynamics in the model, which is beyond the scope of this study.

Milross et al. investigated three different tumour models and found that the necrotic fraction was almost doubled when tumour sizes were increased from 200 mg to 1400 mg.[58] These results are in accordance with our simulations, demonstrating rapidly increasing necrotic fraction. The work by Khalil et al. provided similar results, but with different increments in necrotic fractions.[59] The difference might be caused by differences in oxygen consumption, vascular fraction, blood velocity or vessel architecture used in the models.

In the work by Espinoza et al., the influence of applying variable vascular fraction to a model with a mean pO_2 of 40 mmHg and parallel vessels, was investigated.[60] The results showed that increased variation in VF shifted the oxygen distribution to lower values and slightly increased the hypoxic fraction. However, when the mean oxygen tension was set to values below 30 mmHg, the increase in hypoxic fraction became more pronounced. Their findings also demonstrated the importance of including a continuously declining oxygen tension in the vessels and indicated that the vascular fraction was the parameter with strongest impact on hypoxic fraction. Vascular fractions of 7%, 4%, and 1% were simulated, resulting in hypoxic fractions of around 2%, 35%, and 85%, respectively. We also noticed a similar tendency in our simulations of II, where a decrease in vessel density broadened the distribution, considerably increasing hypoxic fraction, especially in combination with a lowering of blood pO_2 (Figure 4.1).

The impact of vessel architecture on oxygen status and radiosensitivity was inquired into through the variable vascular fraction model, with vascular fractions that increased radially toward the tumour center. The rationale for implementing this model architecture was that a constant reduction in oxygen towards the tumour centre might as well increase angiogenic activity as eliminate tumour tissue due to anoxic cells undergoing apoptosis. These activities would result in increased microvessel density and restored oxygenation.[14] Results were compared to simulations from the constant vascular fraction model but provided only a minor beneficial effect on tumour oxygenation. This seems consistent with the presumed weak oxygen gradient due to the less oxygenated blood of the tumour centre, likely to cause a modest oxygen diffusion.

In the current model, square cross-section vessels, side of 10 μm were used, area-equivalent to a diameter of 11.3 μm in a circular vessel, which was within the smallest known range of tumour vessel dimensions.[61,62] Typically, the small arteries entering a tumour bifurcate successively as they approach the tumour centre, yielding smaller vessels. An experimental study recently demonstrated that the mean vessel diameter of aggressive tumours was 20 μm in the periphery and in the central region, after up to four bifurcations, the mean diameter had dropped to 5 μm.[61] Less aggressive tumours exhibited larger peripheral vessels, undergoing up to eight bifurcations. The inclusion of this type of vessel architecture in our simulations might influence the results. However, based on the minor impact of vessel architecture, it is unlikely that the influence of a more detailed description of vessel size distribution on our results would be of considerable importance.

This model assumed that the vessels were functional, isotropic, evenly distributed, perpendicular to the tumour surface and essentially able to reach the tumour core, when in fact tumour vessels often are leaky, malformed and sometimes even reflected backwards, thereby reducing the number of vessels in the tumour core and thereby the vascular fraction.[63] Intravital microscopy has shown that the vessel arrangement for a breast carcinoma is highly dependent on the host tissue, with organisations ranging from uniform vessel distributions within tumour tissue to a situation with lower vessel density in the tumour core.[63] The latter may be caused indirectly by an increased interstitial pressure, either through compression of the vessels[60] or through induction of necrosis.

For tissue oxygen demand (C_0), a value of 15 mmHg/s was used. The actual consumption varied with oxygen supply in a sense that is likely to reflect the relative metabolic activity of the tissue. Our simulated necrotic fractions, relatively high for large tumours, indicated that the consumption parameters may have been a bit off. Compared to large clinical tumours, the simulated fractions appeared to be overestimated.,[58,59] Possible reasons for overestimation of oxygen consumption are low metabolic activity in living cells and/or overestimation of the number of living cells per volume of tissue.

5.4 Correlation between variables in tumour oxygenation models

This novel Monte Carlo approach manages to generate results for clinically relevant tumour sizes. The overriding factor in determining the time performance of a

numerical model is the number of calculations. This can be strongly modified by including some smart simplifications and carefully selecting methods. Nevertheless, there is a trade-off between accuracy and speed. Accuracy in this situation mainly refers to space and time resolution and tolerance levels. This is a qualitative study and the model is somewhat rough, for example oxygen transport through membranes is excluded as well as the modelling of binding times, environmental factors influencing chemical reactions etcetera. The assumed distributions of model variables are hypothetical estimates and likely to differ between clinical or preclinical situations.

Initially, three parameters were studied in seven scenarios altogether. Positive correlations were examined for all parameter combinations and an invariant scenario, spherically symmetrical and strictly dependent on radial position (DOC) was added as well as a negative correlation (VPO-C). DOC was to represent a perfect angiogenesis situation, where a centrally located hypoxic region was in full control of angiogenesis throughout the tumour. This being unrealistic of course as all clinical situations show variations in biological parameters with location and even time. As the oxygen distributions showed virtually an independence of blood velocity correlations the further studies focused on only three of the correlated scenarios, namely UP, VPO-C and VPO+C plus the invariant DOC scenario. VPO-C, meaning that high vessel proximity occurs together with low oxygen tension and vice versa has an obvious biological relevance as there is a self-regulating function of vessel proximity where there is not enough oxygen to keep the cells functioning, the cells will go into apoptosis, leading to an increased density of vessels.[14] Also the VPO+C scenario, however, can be biologically motivated as there are reports about hypoxic cells reducing their apoptotic potential,[64,65] thereby resisting apoptosis, leading to decreased vessel proximity as proliferation continues close to the vessels,[66,67] while no hypoxic cells are cleared. This pushes the vessels apart and may even clamp them, generating acute hypoxia.[68] If this continues, endothelial cells may actually undergo apoptosis due to hypoxia, which obviously further decreases vessel proximity. All of the scenarios studied have a noticeably log-normal distribution, similar to what we have previously encountered (I,II). Judging from the fractions of hypoxia or necrosis (Figure 4.10), however the ideal scenario seems the most unlikely as large tumours often present considerable volumes of low oxygenation.

It is well established, and supported by our studies, that in general, a smaller tumour

requires a lower absorbed dose for sterilisation. That is because there are fewer tumour cells to kill and it is a natural consequence. Improving tumour oxygenation should decrease the number of hypoxic cells and therefore lower D_{99}. The fluctuating behaviour of D_{99} versus tumour size, mentioned in section 5.3 is highly dependent on the selected threshold separating hypoxia and necrosis, which determines whether a cell is already dead or hard to kill. In this study, the threshold is set to 0 mmHg in order to minimise this effect. We have demonstrated a size-dependent behaviour of hypoxic and necrotic fractions, similar to what has been experimentally observed.[58,59] In the VPO-C scenario, the low values indicate that there is in the interest of the tumours to be able to correlate vessel proximity to oxygen level in this manner in order to grow as big and fast as possible.[69] Analysis of this interplay required the use of physiologically realistic models, which the simplest model was not, due to the constant oxygen levels along the vessels and constant vessel density.

Chapter 6

Conclusions

6.1 Combining antiangiogenic treatment with radionuclides

Adding antiangiogenic drugs to radionuclide treatment is likely to provide increased effect due to the synergistic effects of increased drug uptake and improved oxygenation, leading to a more even dose distribution and a lower average while maintaining or increasing probability of cure and sparing normal tissue. This leaves room for additional treatments. Moreover it is important, in order to make a good estimate of oxygen effective dose, to consider the entire oxygen tension field of the tumour, rather than the hypoxic fraction.

6.2 Modification of blood oxygenation – effects on radiation response

Our modelling results indicate that the effects of a decrease in vessel density, that is, induction of diffusion-limited (chronic) tumour hypoxia, may be neutralised by a comparatively smaller up-regulation in blood oxygen concentration and that an intermediate vascular density region exists where enhanced blood oxygen concentration may be beneficial for radiation response. The distribution characteristics clearly differ between diffusion-limited and anemic hypoxia; the width of the distribution is related to the vessel density but not to oxygen levels in the blood, whereas both forms of hypoxia result in a shift of the entire distribution towards lower values. Therefore, distinguishing between the forms should be possible by studying the pO_2 distribution. However, utilising this potential in the clinical radiotherapy setting remains

a challenge. Recent improvements in assessing tumour hypoxia, such as hypoxia-specific PET imaging,[70,71] may assist in the clinical application of the findings.

6.3 Oxygen variations along vessels – effects on radiation response

As oxygen transport in tissue is mainly driven by concentration gradients, the hypoxia caused by poorly oxygenated blood is not easily compensated by increased vessel density. Information on spatially longitudinal oxygen content variations of the vessels is important as its influence on estimated necrotic fractions and radiosensitivity cannot be neglected, especially for poorly vascularised tumours. The finding that constant vessel pO_2 did not generate necrotic fractions even in large tumours, independent of blood flow, emphasised the inappropriateness of using a mean oxygen tension value to represent the oxygen content of a vessel in calculating tumour oxygenation. Our simulations demonstrated that a model with a constant oxygen level was likely to overestimate radiosensitivity and that, in larger tumours, radiosensitivity did not strictly decrease with increased tumour oxygenation.

6.4 Correlation between variables in tumour oxygenation models

Apparently, blood velocity is the least important parameter, within the ranges studied, when it comes to influencing the oxygen distribution. Of the scenarios studied, a negative correlation between vessel density and pO_2 of the blood (VPO-C) provides by far the best oxygenation conditions for a successful treatment outcome. This scenario has a biological relevance in angiogenesis and the proposed self-regulating vessel spacing, determined by metabolic activity of the tissue.

Chapter 7

Future perspectives

The Achilles' heel of mathematical modelling, a very time and resource efficient tool for gaining knowledge of complex systems, is the lack of distinct connection to reality and therefore the need for validation. Used properly, however, it may provide many valuable insights into, for example, optimisation of cancer treatment. Highly evolved models will undoubtedly be able to improve treatment strategies in the future.

The principal modelling methodology of these studies; involving three-dimensional voxel-based models with a Green's function approach and a touch of Monte Carlo has great potential. It is robust, straight forward, can easily be expanded to problems of different scales and it dodges the problems caused by collapsing the models to two dimensions, as often encountered.

As often in similar situations, one major limitation is computational performance. By using more powerful computers, more sophisticated models can be built, without restraints such as symmetry, modest dimensions, simple boundary conditions and poor time resolution and further details such as extravasation times, convective transport and effects of chemical properties could be included. Modelling performance would be dramatically increased if the models were multi-threaded, that is, split up and simultaneously run piece-wise in parallel on several processors.

As imaging methods improve, more information will be available on distributions of radionuclides. This will further improve modelling results. A more realistic picture of spatial oxygen distributions could be achieved if various vessel sizes and directions were used and branching vessels were investigated in more detail, preferably based on in vivo data. In future studies, model parameter setting should also be improved

using available clinical and pre-clinical information. An interesting aspect would also be to include fractionated radiotherapy in the models, thereby extending the modelled time period and including proliferation as well as temporal variations in vascular and oxygenational properties.

Acknowledgements

This work was supported by grants from the Swedish National Cancer Society, Swedish radiation safety authority, and King Gustav V Jubilee Clinic Cancer Research Foundation.

I am grateful to my main supervisor, professor Peter Bernhardt, for giving me the opportunity to become a Ph.D student, for believing in me, listening to my ideas and helping me navigate when I get lost. We have had many fruitful discussions about research, teenage children and the important topics of life. You have been very kind and a great support. I consider you remarkably clearheaded! I thank my co-supervisors: Dr. Jon Kindblom for encouraging me and taking the time to help making my work medically relevant and for giving valuable input and Dr. Peter Gjertsson for helping me getting started.

I thank my other co-authors Eliane Cortez and professor Kristian Pietras for helping me write a very good article and my fellow Ph.D-students and the staff at the department of radiation physics for making it a good place to work. I also thank the former students at the department, for making me learn by teaching. I thank my brilliant co-workers, who make me want to come to work every day: Tobias Magnander for great company, many laughs and interesting talks, personal and professional, geeky and sometimes ridiculously complex; and Jonas Högberg, probably the best room-mate in the world, for being my friend and for your endless efforts to help me keeping my mind off work. You guys have provided me with the greatest work environment.

I thank my family and relatives for helping me and supporting me in numerous ways.

My final acknowledgement and dedication goes to my lovely, beautiful and gifted children: David, for having a great part in making me who I am and for really taking an interest in what I do; Naima for bringing joy to my life and being so compassionate; Tore for being my favourite buddy who never stands me up or lets me down and Karin, my little sunshine, for constantly reminding me of what is most important and for not taking no for an answer and to my wife, Elin, for always supporting me, for being brutally honest, giving me loads of constructive criticism, helping me keep the balance in life and making me the best I can be, but most of all for giving me this lovely family. You are my best friend and the love of my life!

Jakob H Lagerlöf Värmland, Christmas Eve 2013

Bibliography

[1] G. Box and N. Draper, *Empirical Model-building and Response Surface*. New York, NY, USA: John Wiley & Sons, Inc., 1986.

[2] J. D. Chapman, "Can the two mechanisms of tumor cell killing by radiation be exploited for therapeutic gain?," *J Radiat Res*, vol. 55, no. 1, pp. 2–9, 2014.

[3] E. Hall and A. Giaccia, *Radiobiology for the Radiologist*. Lippincott Williams & Wilkins, 2006.

[4] A. Nias, *An Introduction to Radiobiology*. Wiley, 1998.

[5] D. J. Carlson, R. D. Stewart, and V. A. Semenenko, "Effects of oxygen on intrinsic radiation sensitivity: A test of the relationship between aerobic and hypoxic linear-quadratic (LQ) model parameters," *Med. Phys.*, vol. 33, pp. 3105–15, 2006.

[6] K. Kroy and E. Frey, "Brownian motion: a paradigm of soft matter and biological physics," *Annalen der Physik*, vol. 14, no. 1-3, pp. 20–50, 2005.

[7] A. Einstein, "Über die von der molekularkinetischen Theorie der Wärme geforderte Bewegung von in ruhenden Flüssigkeiten suspendierten Teilchen," *Ann. Phys.*, vol. 322, no. 8, pp. 549–560, 1905.

[8] B. Wang, J. Kuo, S. Bae, and S. Granick, "When Brownian diffusion is not Gaussian," *Nat Mater*, vol. 11, pp. 481–485, June 2012.

[9] A. Fick, "Über Diffusion," *Annalen der Physik und Chemie*, vol. 170, no. 1, pp. 59–86, 1855.

[10] T. S. Ursell, "The Diffusion Equation - A Multi-dimensional Tutorial.".

[11] J. Hall and A. Guyton, *Textbook of medical physiology*. Guyton Physiology Series, Elsevier Saunders, 2006.

[12] J. West, *Respiratory Physiology, 9th Ed.* Lippincott Williams & Wilkins, 2012.

[13] R. Law and H. Bukwirwa, "The Physiology of Oxygen Delivery," 1999.

[14] L. Hlatky, P. Hahnfeldt, and J. Folkman, "Clinical application of antiangiogenic therapy: microvessel density, what it does and doesn't tell us.," *Journal of the National Cancer Institute*, vol. 94, pp. 883–893, June 2002.

[15] V. Kumar, N. Fausto, and A. Abbas, *Robbins & Cotran Pathologic Basis of Disease, Seventh Edition*. Saunders, 7 ed., July 2004.

[16] R. K. Jain, E. di Tomaso, D. G. Duda, J. S. Loeffler, A. G. Sorensen, and T. T. Batchelor, "Angiogenesis in brain tumours," *Nat Rev Neurosci*, vol. 8, no. 8, pp. 610–22, 2007.

[17] E. Mehrara, E. Forssell-Aronsson, H. Ahlman, and P. Bernhardt, "Specific growth rate versus doubling time for quantitative characterization of tumor growth rate.," *Cancer research*, vol. 67, no. 8, pp. 3970–3975, 2007.

[18] A. Hertig, *Angiogenesis in the Early Human Chorion and in the Primary Placenta of the Macaque Monkey*. Carnegie Institution of Washington publication, 1935.

[19] K. Pietras, A. Östman, M. Sjöquist, E. Buchdunger, R. Reed, C.-H. Heldin, and K. Rubin, "Inhibition of platelet-derived growth factor receptors reduces interstitial hypertension and increases transcapillary transport in tumors.," *Cancer Res*, vol. 61, pp. 2929–, 2001.

[20] C. Lee, M. Heijn, E. di Tomaso, G. Griffon-Etienne, M. Ancukiewicz, C. Koike, K. Park, N. Ferrara, R. Jain, H. Suit, and Y. Boucher, "Anti-Vascular endothelial growth factor treatment augments tumor radiation response under normoxic or hypoxic conditions.," *Cancer research*, vol. 60, pp. 5565–5570, Oct. 2000.

[21] R. Jain, R. Tong, and L. Munn, "Effect of vascular normalization by antiangiogenic therapy on interstitial hypertension, peritumor edema, and lymphatic metastasis: insights from a mathematical model.," *Cancer Res*, vol. 67, pp. 2729–2735, Mar. 2007.

[22] F. Winkler, S. V. Kozin, R. T. Tong, S. S. Chae, M. F. Booth, I. Garkavtsev, L. Xu, D. J. Hicklin, D. Fukumura, E. di Tomaso, L. L. Munn, and R. K. Jain, "Kinetics of vascular normalization by VEGFR2 blockade governs brain tumor response to radiation: role of oxygenation, angiopoietin-1, and matrix metalloproteinases," *Cancer Cell*, vol. 6, no. 6, pp. 553–63, 2004.

[23] R. Eckhardt, "Stan Ulam, John von Neumann, and the Monte Carlo method," *Los Alamos Science*, vol. 15, pp. 131–136, 1987.

[24] G. Arfken, H. Weber, and F. Harris, *Mathematical Methods for Physicists, Sixth Edition: A Comprehensive Guide*. Academic Press, 6 ed., July 2005.

[25] J. James, *A Student's Guide to Fourier Transforms: With Applications in Physics and Engineering*. Cambridge University Press, 2002.

[26] B. Romenij, *Front-End Vision and Multi-Scale Image Analysis*. Kluwer Academic, 2003.

[27] V. Tutatchikov, O. Kiselev, and M. Noskov, "Calculating the n-dimensional fast fourier transform," *Pattern Recognition and Image Analysis*, vol. 23, no. 3, pp. 429–433, 2013.

[28] T. Kayama, T. Yoshimoto, S. Fujimoto, and Y. Sakurai, "Intratumoral oxygen pressure in malignant brain tumor," *J Neurosurg*, vol. 74, no. 1, pp. 55–9, 1991.

[29] J. Kirkpatrick, L. Cardenas-Navia, and M. Dewhirst, "Predicting the effect of temporal variations in pO_2 on tumor radiosensitivity," *Int. J.Radiat. Oncol., Biol., Phys.*, vol. 59, no. 3, p. 822–833, 2004.

[30] H. Uusijarvi, N. Chouin, P. Bernhardt, L. Ferrer, M. Bardies, and E. Forssell-Aronsson, "Comparison of electron dose-point kernels in water generated by the Monte Carlo codes, PENELOPE, GEANT4, MCNPX, and ETRAN," *Cancer biotherapy and radiopharmaceuticals*, vol. 24, no. 4, pp. 461–7, 2009.

[31] C. J. Z. M. Berger, M.J. and J. Chang, "ESTAR, PSTAR, and ASTAR: Computer Programs for Calculating Stopping-Power and Range Tables for Electrons, Protons, and Helium Ions (version 1.2.3)," 2005.

[32] P. Bernhardt, H. Ahlman, and E. Forssell-Aronsson, "Model of metastatic growth valuable for radionuclide therapy," *Med Phys*, vol. 30, no. 12, pp. 3227–32, 2003.

[33] J. R. Williams, Y. Zhang, H. Zhou, D. S. Gridley, C. J. Koch, J. Russell, J. S. Slater, and J. B. Little

[34] D. Hanahan, "Heritable formation of pancreatic beta-cell tumours in transgenic mice expressing recombinant insulin/simian virus 40 oncogenes," *Nature*, vol. 315, no. 6015, pp. 115–22, 1985.

[35] Secomb, T. W. and Hsu, R. and Dewhirst, M. W. and Klitzman, B. and Gross, J. F., "Analysis of oxygen transport to tumor tissue by microvascular networks," *International journal of radiation oncology, biology, physics*, vol. 25, no. 3, pp. 481–9, 1993.

[36] A. Dasu, I. Toma-Dasu, and M. Karlsson, "Theoretical simulation of tumour oxygenation and results from acute and chronic hypoxia," *Physics in medicine and biology*, vol. 48, no. 17, pp. 2829–42, 2003.

[37] L. Michaelis and M. L. Menten, "Die Kinetik der Invertinwirkung," *Biochemische Zeitschrift*, vol. 49, pp. 333–369, 1913.

[38] I. F. Tannock, "Oxygen diffusion and the distribution of cellular radiosensitivity in tumours," *The British journal of radiology*, vol. 45, no. 535, pp. 515–24, 1972.

[39] R. Thomlinson and L. H. Gray, "The histological structure of some human lung cancers and the possible implications for radiotherapy," *Br J Cancer*, vol. 9, no. 4, p. 539–549, 1955.

[40] J. Severinghaus, "Simple, accurate equations for human blood O_2 dissociation computations," *Appl. Physiol. Respir. Environ. Exerc. Physiol.*, vol. 46, pp. 599–602, 1979.

[41] O. Ndubuizu and J. C. LaManna, "Brain tissue oxygen concentration measurements," *Antioxid Redox Signal*, vol. 9, no. 8, pp. 1207–19, 2007.

[42] W. R. Ott, "A physical explanation of the lognormality of pollutant concentrations," *J Air Waste Manage Assoc*, vol. 40, no. 10, pp. 1378–83, 1990.

[43] P. V. Neti and R. W. Howell, "Log normal distribution of cellular uptake of radioactivity: implications for biologic responses to radiopharmaceuticals," *Journal of nuclear medicine : official publication, Society of Nuclear Medicine*, vol. 47, no. 6, pp. 1049–58, 2006.

[44] V. P. Antipas, G. S. Stamatakos, N. K. Uzunoglu, D. D. Dionysiou, and R. G. Dale, "A spatio-temporal simulation model of the response of solid tumours to radiotherapy in vivo: parametric validation concerning oxygen enhancement ratio and cell cycle duration," *Phys Med Biol*, vol. 49, no. 8, pp. 1485–504, 2004.

[45] J. Z. Wang, X. A. Li, and N. A. Mayr, "Dose escalation to combat hypoxia in prostate cancer: a radiobiological study on clinical data," *Br J Radiol*, vol. 79, no. 947, pp. 905–11, 2006.

[46] A. E. Nahum, B. Movsas, E. M. Horwitz, C. C. Stobbe, and J. D. Chapman, "Incorporating clinical measurements of hypoxia into tumor local control modeling of prostate cancer: implications for the alpha/beta ratio," *Int J Radiat Oncol Biol Phys*, vol. 57, no. 2, pp. 391–401, 2003.

[47] G. S. Stamatakos, V. P. Antipas, N. K. Uzunoglu, and R. G. Dale, "A four-dimensional computer simulation model of the in vivo response to radiotherapy of glioblastoma multiforme: studies on the effect of clonogenic cell density," *Br J Radiol*, vol. 79, no. 941, pp. 389–400, 2006.

[48] D. W. Lübbers, *The meaning of tissue oxygen distribution curves and its measurement by means of platinum electrodes.*, vol. 3, p. 12. New York: S. Karger, 1969.

[49] G. A. Kaltsas, D. Papadogias, P. Makras, and A. B. Grossman, "Treatment of advanced neuroendocrine tumours with radiolabelled somatostatin analogues," *Endocr Relat Cancer*, vol. 12, no. 4, pp. 683–99, 2005.

[50] S. J. Goldsmith, "Radioimmunotherapy of lymphoma: Bexxar and Zevalin," *Semin Nucl Med*, vol. 40, no. 2, pp. 122–35, 2010.

[51] H. Ahmadzadehfar, H. J. Biersack, and S. Ezziddin, "Radioembolization of liver tumors with yttrium-90 microspheres," *Semin Nucl Med*, vol. 40, no. 2, pp. 105–21, 2010.

[52] A. Dasu, I. Toma-Dasu, and M. Karlsson, "The effects of hypoxia on the theoretical modelling of tumour control probability," *Acta oncologica*, vol. 44, no. 6, pp. 563–71, 2005.

[53] C. W. Chiu, H. Nozawa, and D. Hanahan, "Survival benefit with proapoptotic molecular and pathologic responses from dual targeting of mammalian target of rapamycin and epidermal growth factor receptor in a preclinical model of pancreatic neuroendocrine carcinogenesis," *J Clin Oncol*, vol. 28, no. 29, pp. 4425–33, 2010.

[54] P. Vaupel and A. Mayer, "Hypoxia in cancer: significance and impact on clinical outcome," *Cancer Metastasis Rev*, vol. 26, no. 2, pp. 225–39, 2007.

[55] P. Vaupel, A. Mayer, and M. Hockel, "Impact of hemoglobin levels on tumor oxygenation: the higher, the better?," *Strahlenther Onkol*, vol. 182, no. 2, pp. 63–71, 2006.

[56] C. M. Hoff, "Importance of hemoglobin concentration and its modification for the outcome of head and neck cancer patients treated with radiotherapy," *Acta Oncol*, vol. 51, no. 4, pp. 419–32, 2012.

[57] C. Lo Nigro, M. Maffi, J. Fischel, M. Monteverde, P. Catarsi, F. Tonissi, L. Lattanzio, M. Riba, M.-C. Etienne-Grimaldi, P. Formento, G. Milano, and M. Merlano, "Impact of erythropoietin on the effects of irradiation under hypoxia," *Journal of Cancer Research and Clinical Oncology*, vol. 135, no. 11, pp. 1615–1623, 2009.

[58] C. Milross, S. Tucker, K. Mason, N. Hunter, L. Peters, and L. Milas, "The effect of tumor size on necrosis and polarographically measured pO_2," *Acta Oncol.*, vol. 36, pp. 283–189, 1995.

[59] A. Khalil, M. Horsman, and O. J., "The importance of determining necrotic fraction when studying the effect of tumour volume on tissue oxygenation," *Acta Oncol.*, vol. 34, no. 3, pp. 297–300, 1995.

[60] I. Espinoza, P. Peschke, and C. P. Karger, "A model to simulate the oxygen distribution in hypoxic tumors for different vascular architectures," *Med. Phys.*, vol. 40, p. 081703, 2013.

[61] J. Ehling, B. Theek, F. Gremse, S. Baetke, D. Möckel, J. Maynard, S. A. Ricketts, H. Grüll, M. Neeman, R. Knuechel, W. Lederle, F. Kiessling, and T. Lammers, "Micro-CT imaging of tumour angiogenesis," *Journal of Pathology*, vol. 184, pp. 431–41, 2013.

[62] M. Dewhirst, C. Y. Tso, R. Oliver, C. S. Gustafson, T. W. Secomb, and J. F. Gross, "Morphologic and hemodynamic comparison of tumor and healing normal tissue microvasculature," *Int. J.Radiat. Oncol., Biol., Phys.*, vol. 17, pp. 91–99, 1989.

[63] B. J. Vakoc, R. M. Lanning, J. A. Tyrrell, T. P. Padera, L. A. Bartlett, T. Stylianopoulos, L. L. Munn, G. J. Tearney, D. Fukumura, R. K. Jain, and B. E. Bouma, "Three-dimensional microscopy of the tumor microenvironment in vivo using optical frequency domain imaging," *Nature Medicine*, vol. 15, no. 10, 2009.

[64] T. G. Graeber, C. Osmanian, T. Jacks, D. E. Housman, C. J. Koch, S. W. Lowe, and A. J. Giaccia, "Hypoxia-mediated selection of cells with diminished apoptotic potential in solid tumours," *Nature*, vol. 379, no. 6560, pp. 88–91, 1996.

[65] M. Kilic, H. Kasperczyk, S. Fulda, and K.-M. Debatin, "Role of hypoxia inducible factor-1 alpha in modulation of apoptosis resistance.," *Oncogene*, vol. 26, no. 14, pp. 2027–38, 2007.

[66] J. T. Erler, C. J. Cawthorne, K. J. Williams, M. Koritzinsky, B. G. Wouters, C. Wilson, C. Miller, C. Demonacos, I. J. Stratford, and C. Dive

[67] E. C. Finger and A. J. Giaccia, "Hypoxia, inflammation, and the tumor microenvironment in metastatic disease.," *Cancer Metastasis Rev*, vol. 29, no. 2, pp. 285–93, 2010.

[68] T. W. Secomb, J. P. Alberding, R. Hsu, M. W. Dewhirst, and A. R. Pries, "Angiogenesis: An Adaptive Dynamic Biological Patterning Problem," *PLoS Comput Biol*, vol. 9, 03 2013.

[69] I. Tannock and I. Kopelyan, "Variation of pO_2 in the growth medium of spheroids: interaction with glucose to influence spheroid growth and necrosis," *Br J Cancer*, vol. 53, no. 6, p. 823–827, 1986.

[70] V. R. Bollineni, E. M. Wiegman, J. Pruim, H. J. Groen, and J. A. Langendijk, "Hypoxia imaging using Positron Emission Tomography in non-small cell lung cancer: Implications for radiotherapy," *Cancer Treat Rev*, 2012.

[71] H. Kurihara, N. Honda, Y. Kono, and Y. Arai, "Radiolabelled agents for PET imaging of tumor hypoxia," *Curr Med Chem.*, vol. 19, no. 20, 2012.